Title
A Novel Excitation Scheme for an Ocean Wave Energy Converter

Author
Orazov, Bayram

Publication Date
2011

Peer reviewed|Thesis/dissertation

A Novel Excitation Scheme for an Ocean Wave Energy Converter

by

Bayram Orazov

A dissertation submitted in partial satisfaction of the

requirements for the degree of

Doctor of Philosophy

in

Engineering – Mechanical Engineering

in the

Graduate Division

of the

University of California, Berkeley

Committee in charge:

Professor Oliver M. O'Reilly, Co-Chair
Professor Ömer Savaş, Co-Chair
Professor Mark Stacey

Fall 2011

A Novel Excitation Scheme for an Ocean Wave Energy Converter

Abstract

A Novel Excitation Scheme for an Ocean Wave Energy Converter

by

Bayram Orazov

Doctor of Philosophy in Engineering − Mechanical Engineering

University of California, Berkeley

Professor Oliver M. O'Reilly, Co-Chair

Professor Ömer Savaş, Co-Chair

This dissertation presents a design for a novel water intake mechanism for a buoy-type ocean wave energy converter (WEC). These renewable energy-harvesting devices float in the open sea and are set into vertical oscillatory motion by incident ocean waves, extracting energy from the relative motion of two or more component bodies. Energy extraction in a WEC can be performed by a variety of power takeoff systems (PTO), such as hydraulic, overhead turbines, or linear magnet generators. The work presented in this dissertation is concerned with improving the power harnessing capabilities of buoy-type WECs. To this end, we propose a novel mass modulation scheme and present designs for the associated water intake mechanism. The water intake mechanism traps and releases surrounding water as needed, thereby leading to a variation of the system's mass. The mass modulation is designed to improve the power harnessing potential of a WEC by varying the system mass at a rate of twice the frequency of the incident ocean waves.

To investigate the feasibility of the mass modulation scheme, a simple numerical model for a WEC equipped with the water intake mechanism is proposed and analyzed. Of particular interest is the relationship between mass modulation and energy harvesting, as well as the stability implications for the WEC of such a mass variation. The motions of the system have been studied in response to a spectrum of harmonic excitation and the results were catalogued. Numerical simulations have also been used to demonstrate that when applied correctly, mass modulation can lead to a significant increase in system response and power harnessing potential of a WEC.

A scale prototype of a WEC with the water intake mechanism has been constructed and tested in a wave tank to prove the concept of the proposed mass modulation scheme. The results presented in this dissertation show that a WEC fitted with the water intake mechanism exhibits a higher vertical velocity response, compared to a non-mass modulated WEC. In addition, the relative velocity between the WEC and a secondary float can also be

increased using the mass modulation. These velocity increases can lead to improvements in the power harnessing potential of the WEC.

Contents

Acknowledgments

Large portions of the work presented in this dissertation were made possible by funding from the U. S. National Science Foundation through grant number CMMI-1000906 and a grant from the UCB-KAUST Academic Excellence Alliance. I would also like to acknowledge the constructive criticisms of the anonymous reviewers for the papers [21] and [22] that I coauthored and which form central components for this dissertation.

This thesis presents the work that was influenced, directly or indirectly, by a number of people that I would like to specifically express my gratitude to.

I wish to thank Professor Oliver M. O'Reilly, my academic and research advisor through my entire graduate career. Without his guidance, inspiration and help this research simply would not have happened.

My thanks also go to Professor Ömer Savaş, who has co-advised this research and have proven absolutely invaluable in the experimental aspects of the work presented here. Both Professors O'Reilly and Savaş have been a sheer pleasure to work with on a technical and personal levels alike. I could not have asked for a better team of advisors.

A special thanks goes to Professor Mark Stacey of Civil and Environmental Engineering at UC Berkeley.

I would also like to thank Xuance Zhou for his help in determining system stability, presented in Chapter 3 of this dissertation.

The construction of the scale prototype would not have been possible without the help and excellent advice of the UC Berkeley Mechanical Engineering Machine Shop staff - El Bennett, Mick Franssen, Gordon Long, Scott McCormick and Wendy Penning. What I learned about design and engineering from working with these people is hard to overstate. It is a skill set that I hope to use for the rest of my life. Thanks to them, I now dream of owning my own lathe, mill and a few other shop tools.

The necessary background to undertake the work presented here would have been lacking, have I not received a world class undergraduate and graduate education in the Mechanical Engineering department at UC Berkeley. For that I wish to thank all of my past professors and the department staff. I would particularly like to acknowledge Professors George C. Johnson, Benson H. Tongue, Ronald W. Yeung, and Tarek I. Zohdi.

Most of all, I wish to thank my parents for the support and understanding they have given me throughout my life.

Chapter 1

An Introduction to Ocean Wave Energy

1.1 The Wave Energy Resource

As the humankind is becoming increasingly concerned with environmental impacts of energy generation, the importance of clean, renewable energy sources cannot be overstated. And while wind and solar energy have perhaps stolen the spotlight in recent years, it is, in fact, the ocean waves that offer the greatest potential. The latter is recognized to contain the highest energy density among renewables, its concentration is very predictable and the resource itself is virtually inexhaustible.

There are a number of ways in which ocean waves can be generated. The most common waves, and the ones relied upon for energy generation, result from the blowing of the winds across the sea surface. But since winds arise from the differential heating of the earth by the sun, these ocean waves can be considered a concentrated form of solar energy. Original solar power levels of ≈ 100 W/m^2 can be transformed into waves of power levels of ≈ 1000 W/m of crest length. Other sources of wave generation are storms, tsunamis, and Sun and Moon effects (tides). Each group has a characteristic period range, which is illustrated in Fig. 1, along with the relative energy carried by these waves.

Since waves lose energy due to friction with the ocean floor, off-shore (10 km or more away from coast) ocean regions have higher energy concentration than do shore or near-shore regions. The global exploitable off-shore resource is estimated to be around 2000 TW [1]. To put these numbers in perspective, in 2005 the U.S. Department of Energy reported that the total U.S. energy consumption was around 3.3 TW[1]. Fig. 2 shows average annual wave power levels along coasts around the world, and it is general consensus that regions with power levels over 15 kW/m of wave crest length should have the potential to generate energy at prices competitive with fossil fuels. It should be noted that the current prices of energy produced using fossil fuels do not internalize the cost of negative environmental impacts associated with such methods of energy generation. In effect, this makes the alternative energy sources appear less affordable.

[1] http://www.eia.doe.gov/emeu/aer/consump.html

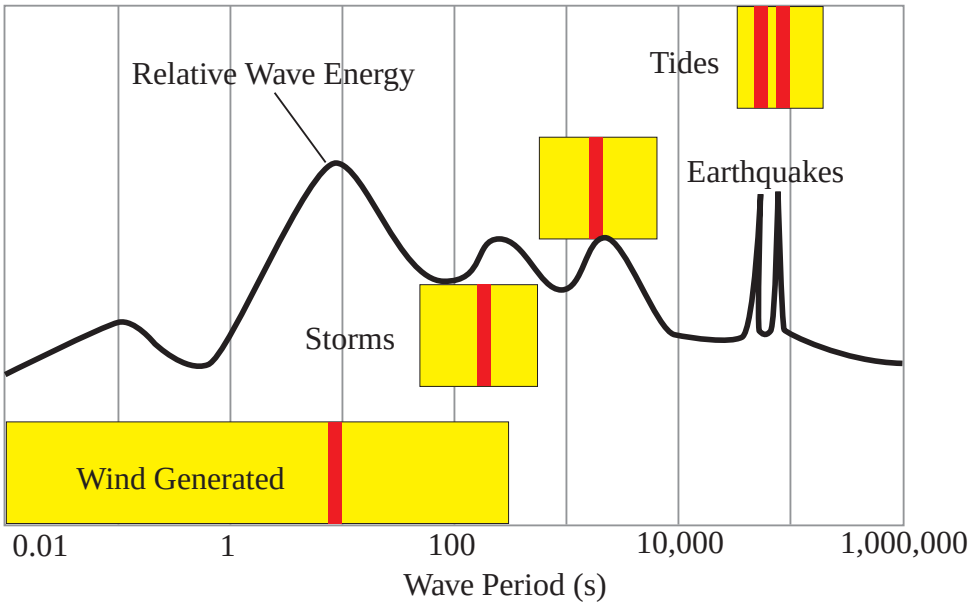

Fig. 1 Ocean waves classified by their origin and relative power levels [2]. Yellow bars denote the range of frequencies, while red bars indicate the mean period for each type of wave. Wave power levels courtesy of NOAA (co-ops.nos.noaa.gov/levelhow.html)

1.2 Wave Energy Conversion Technology

The first widely acknowledged impetus to development of ocean wave energy converters (WECs) has been a spike in the price of coal in the 19th century, although the first known patent in the field dates back to 1799, filed by Girard and Son in France [6]. Between 1855 and 1973 there were 340 patents relating to wave power [16]. However, it took the 1973 oil crisis to put ocean waves on the map as a viable energy source. Over the past 30 years, WEC technology has seen an increase in the pace of development with a multitude of new designs, most of which have originated in Europe. Due to a number of circumstances, only a few technologies have reached a stage of mature prototypes. Below is a listing of primary types of WECs.

- **Oscillating Water Column (OWC)** - the rising and falling of the water level due to waves moves an enclosed column of air above the water. The resulting air flow typically drives a generator turbine. While OWCs can be implemented on-shore, near-shore, and off-shore, the size and cost issues associated with such devices may limit their use in open seas. The majority are constructed as permanent, on-shore installations.

- **Overtopping Device (OTD)** - water is captured from incoming waves and stored in a reservoir above the sea level. This water is then returned to the sea through low-

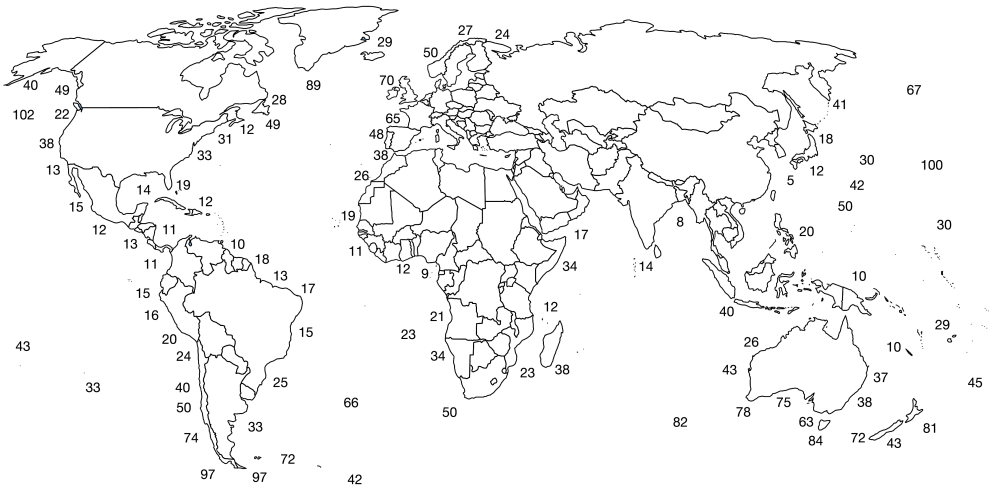

Fig. 2 Average annual wave power levels as kW/m of wave front around the world. Source: www.pelamiswave.com

head turbines that generate power. OTDs are well suited for use in open seas with significant wave amplitudes.

- **Wave Activated Body (WAB)** - waves force the device into oscillatory motions (mainly heave, pitch and roll; surge-based devices also exist) relative to a separate fixed body or between parts of the device. A power takeoff system (PTO) - mechanical, hydraulic or electric - uses these motions to drive a generator. Because WABs rely on excitation via oncoming waves, these devices must be deployed off-shore to harness significant energy.

Figure 3 illustrates an example of each type. Additionally, wave activated bodies can be categorized based on their size and orientation relative to the waves as follows:

- **Point Absorber** - physical dimensions are small compared to the dominant wavelength; can capture energy from waves in any direction.
- **Terminator** - principal axis is parallel to the incident wave crest, terminating the wave; captures energy only from waves traveling in a specific direction.
- **Attenuator** - principal axis parallel to the direction of the incoming wave; captures energy only from waves traveling in a specific direction.

Typically, point absorbers are more compact (and cheaper) than terminators or attenuators. On the other hand, terminators and attenuators tend to have a broader resonant bandwidth than point absorbers, which allows them to harness energy from a broader range

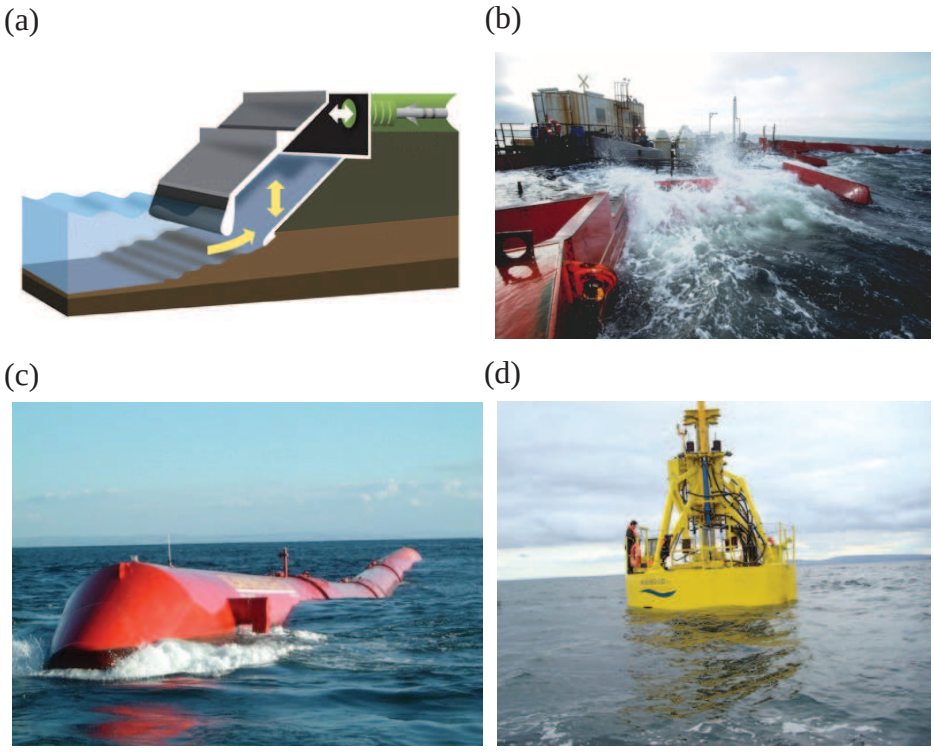

Fig. 3 Examples of wave energy converters: (a) schematic of an oscillating water column (photo: MIT); (b) Wave Dragon, an overtopping device (photo: Wave Dragon); (c) Pelamis, an attenuator (photo: Pelamis); (d) Wavebob, a heaving buoy point absorber (photo: WaveBob)

of wave frequencies. However, when a point absorber is operated in a controlled mode, this disadvantage can be eliminated by tuning the absorber's natural frequency to match the dominant wave frequency.

1.3 Heaving Buoys

Because the work presented below focuses on heaving buoys, it is useful to describe these devices in more detail. Heaving buoys work by being forced into vertical heaving motion by the passing waves. Unlike signal buoys used in the sea, the WEC buoys usually have an underwater mass (distinct from the mooring system), connected to the surface float, which is excited by the waves. Because of this underwater mass, the float does not simply follow the vertical profile of the wave, but actually moves above and below the water surface. However, due to the system's inertia, the waves are not able to force the buoy into such an oscillatory motion if the excitation frequency is too far away from the buoy's natural frequency. Sea waves typically contain several harmonics. The harmonic with the highest amplitude is known as the dominant harmonic, and is referred to whenever

the excitation frequency is mentioned subsequently. A natural frequency of the oscillator is traditionally defined as

$$\omega_n = \sqrt{\frac{k}{m}}, \tag{1.1}$$

where k is the spring constant and m is the oscillator's mass. In the case of a WEC buoy the spring constant arises from the restoring force of the water, i.e. buoyancy, and is generally volume dependent and therefore fixed. To ensure that the buoy is excited by the waves at all times, it is therefore desirable to adjust the mass of the buoy to match ω_n to the frequency of the dominant harmonic in the wave. Such adjustment is used in the Wavebob[2] WEC, which uses underwater tanks that can be partially or fully filled with water to alter the natural frequency of the device. Furthermore, instead of a single float, Wavebob utilizes two floats - an inner and an outer one, as illustrated in Fig. 4, each with a corresponding mass adjustment mechanism. When excited by the waves, the two floats move out of phase with each other. A hydraulic power take off system (PTO), connected between the floats, utilizes the relative motion of the floats to harness energy.

Because of the nature of sea wave climate, the dominant harmonic of the waves often stays constant for hours on end. Thus, the mass adjustments in the Wavebob need not be frequent. A system of pumps is well suited for such application.

1.4 Tidal Energy

Often mistakenly associated with ocean wave energy, tidal is a separate renewable energy resource that has been exploited in select locations for the past millennium. Tides are generated by Earth-Moon and Earth-Sun gravity. As such, their occurrence, direction and magnitude are very predictable.

The earliest known example of tidal energy harvesting dates back to 787AD in the form of the Nendrum Monastery tidal mill on an island in Northern Ireland, although there is some evidence [28] that an even earlier mill may have been constructed in London around 100AD. These mills operate as follows. A dam with a sluice is constructed across a tidal inlet, such as a river estuary. When the tide rises, it fills the mill pond with water. Once the tide gets low enough, the stored water can be used to turn a water wheel. Modern methods of tidal energy harvesting are barraging and tidal stream turbines, illustrated in Fig. 5

Barrages are, effectively, modern versions of tidal mills. Barrages are built across a bay or a river and contain turbines within the barrage walls. These operate similar to a hydro dam. When the water level on one side of the barrage is significantly higher than on the other side, water is allowed to flow across the barrage turning the turbines. Needless to say, such plants are expensive to construct, although the running costs are low. The largest barrage power plant in existence is situated on the Rance river in France. It has a rating of

[2] http://www.wavebob.com

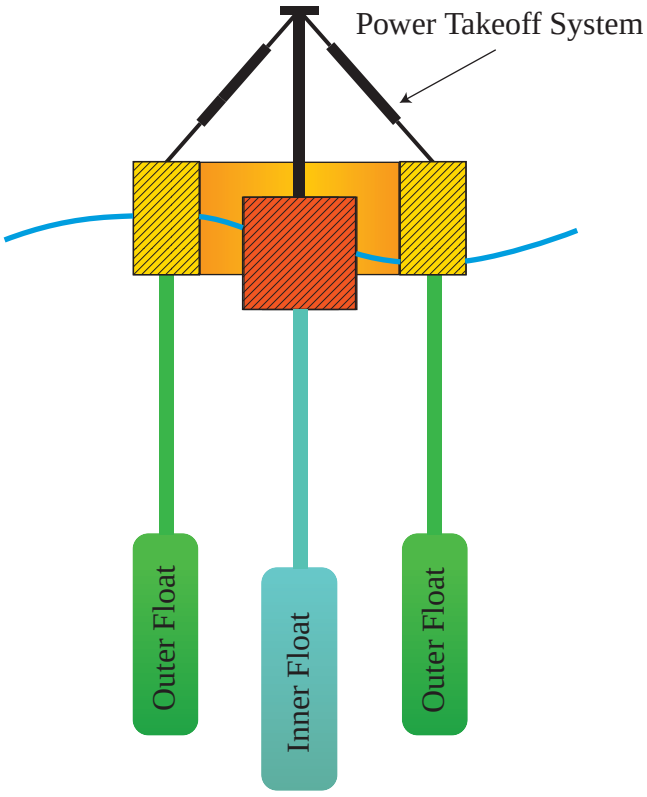

Fig. 4 Schematic of the Wavebob wave energy converter. The relative motion of the inner and outer floats is used to harness energy

(a) (b)

Fig. 5 Two of the most prominent tidal energy converters: (a) Rance river barrage plant in France (photo: WikiMedia Commons); (b) Illustration of the SeaGen tidal turbine installed in Northern Ireland (photo: Marine Current Turbines)

240MW and has been operational since 1966 with an average annual output of around 600 GWh. Two smaller barrage plants exist in the Bay of Fundy, Canada and in Kislaya Guba, Russia.

Tidal stream turbines is a relatively modern approach to tidal energy harvesting and is growing in popularity. The concept is akin to wind turbines, but installed underwater in direct path of the tidal current. Both axial and vertical axis turbines are being developed. To date, the first and only commercial tidal turbine, SeaGen, has been installed in Strangford Lough in Northern Ireland. SeaGen is manufactured by Marine Current Turbines. It has been operational since July 2008 and supplies 1.2MW of power to the grid between 18 and 20 hours per day.

1.5 Outline of the Thesis

With this research effort, we attempt to improve the energy harvesting capabilities of WECs in general, and heaving buoys, such as Wavebob, in particular. We extend the concept of a heaving buoy to include passive modulation of the system mass using a novel water intake system that is presented in Chapter 2. The addition of a time varied mass places our system into the class of hybrid systems and has the effect of parametric-like resonance that increases the heaving amplitude. This behavior and its effect on system stability is explored using a single-degree-of-freedom numerical model in Chapter 3. Using the findings from Chapter 3, an experimental prototype of a wave energy converter has been constructed and tested in a tow-tank. The results of this experimental work are shown in

Chapter 4. Finally, Chapter 5 concludes the thesis with a summary of the performed work and discusses the future direction of this research.

Chapter 2

The Novel Water Intake System

The ultimate goal of this research is to devise a way of improving energy harvesting potential of heaving buoys using the incident ocean waves. In this chapter we propose a completely novel concept of doing this by means of passive, state dependent mass modulation of the buoy system. We first review the concept of parametric resonance, which served as the motivation for the development of this idea. Following that, we propose the mass modulation scheme and the associated mechanism that passively exploits ocean waves to trap and release the water inside the system.

2.1 Parametric Excitation

Before we discuss the novel water intake system presented below, a motivation for such development is in order. This motivation stems from examining the concept of parametric excitation and the effects it can have on an oscillating system. Dating to the seminal paper by Rugar and Grütter [26], it has been known that parametric excitation can produce mechanical amplification in the response of a resonator. This amplification has been used in a variety of MEMS oscillators (see [23] and references therein), and has also been discussed for use in an oscillating water column WEC [20]. In its basic form, parametric excitation occurs when the value of the energy storing parameter(s) of an oscillator is (are) varied in time. When the variation occurs at the right rate and phase, parametric resonance can take place, which increases the oscillation amplitude of the system. In a typical mechanical oscillator the energy is stored via inertia (mass, mass moment of inertia) and stiffness (spring constant). The strongest amplitude amplification will occur if one of the above parameters is varied at twice the natural frequency of the system. This is known as the primary parametric resonance. The amplification, albeit to a smaller extent, is possible at other modulation frequencies, provided they satisfy

$$\omega = 2\omega_n/n, \quad n = 1,2,3,\ldots, \tag{2.1}$$

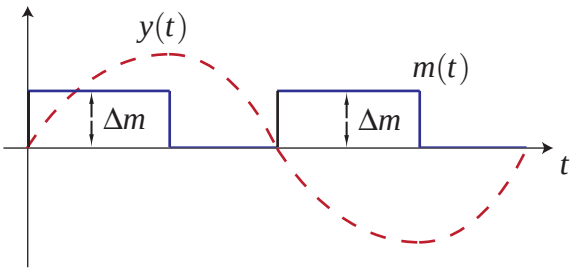

Fig. 6 The vertical motion of the system $y(t)$ shown with a dashed line, while the mass modulation $m(t)$ is shown with a solid line. When $m(t) = 0$, no mass is being added to the default system mass M

where ω is the frequency of parameter modulation and ω_n is the system's natural frequency of oscillation. Physically, the conditions on parametric resonance are such that over an oscillation cycle there occurs a positive energy input into the system. This guides the timing of parameter variation relative to the system's motion. Further information on parametric excitation can be found in [3–5, 30] and references therein.

2.2 The Novel Water Intake System

Building on Wavebob's idea of mass adjustments and the parametric excitation theory, we propose a novel water intake system that connects to the surface float and passively varies the system's mass at twice its oscillating frequency to increase the oscillation amplitude and improve energy harvesting capabilities of a WEC. The water intake system was first proposed in [21] and mimics square wave modulation of the mass of the system by trapping water for the first quarter of the periodic motion, releases it for the second quarter, traps it for the third quarter, and releases the water again for the fourth quarter of the motion. The nature of the excitation is thus similar to parametric, since the energy storing parameter (mass) is varied at twice the motion frequency, but differs from it because the parameter switching is state-dependent. In other words, the changes to the mass occur based on the position and velocity of the system, instead of fixed timing. Therefore, the system belongs to a class of switched systems. Fig. 6 illustrates the scheme.

Referring to Fig. 7, the water intake system is comprised of a submerged (at all times) hollow cylinder labeled (2) in Fig. 7, open at both ends and rigidly attached to the surface float (1) that is excited by the waves. Inside the cylinder, located near its vertical midpoint (3), are two pairs of centrally hinged butterfly flaps. The upper flaps (4) are able to swing between horizontal and vertical up positions, while the lower flaps (5) can only swing between horizontal and vertical down positions. The exact vertical orientations would depend on system design considerations, such as geometry and drag vs. sensitivity tradeoff.

When in the horizontal 'closed' position, each pair of flaps covers the entire cross section of the cylinder, thereby blocking off water flow through the inside of the cylinder. As

water cannot flow through the cylinder, it gets trapped in both of its halves, thereby creating the desired added mass effect. The reason the water gets trapped is as follows. In the first quarter cycle when the system is moving up, the water in the top half of the hollow cylinder (2) is effectively scooped up and has nowhere to flow. It therefore becomes a part of the system. At the same time, the water in the lower half has nowhere to flow either, because the cross section of the cylinder is blocked off, and the water surrounding the cylinder is under greater pressure (atmospheric and hydrostatic) than the water in the lower half of the cylinder. Effectively, a vacuum state is created in the lower half of the cylinder when the top flaps are closed, which holds the water in. In the third quarter cycle when the system is moving down, the effects are reversed and the 'vacuum' state is created in the upper half of the cylinder, while the water in the lower half is scooped up.

It should be noted that the mechanism is arranged in such a way as to allow at most one set of flaps to be closed at any given time. The remaining parts of the water intake system, as labeled in Fig. 7, are the horizontal plates (6), sliding on the outside of, and relative to, the cylinder due to water pressure from the top or bottom, depending on the direction of motion. When passing through the midpoint (3) of the cylinder, the sliding plates can lock or unlock the flaps (4) or (5) in their 'open' configurations. In Fig. 7 the locked state is indicated by an arc between the flaps. The locking mechanism can range from a simple mechanical latch to an electronically controlled brake. Our solution is discussed in Chapter 4.

During a typical period of the system's motion (shown as a dashed sine wave), the water intake operates as follows. At point labeled *a* in Fig. 7 the sliding plates (6) pass through the midpoint (3) of the cylinder, locking lower flaps (5) in the open configuration and unlocking upper flaps (4) from their previously open configuration. Because the cylinder is moving up, the water pressure above the upper flaps is greater than below them. This forces the upper flaps to swing downward into the horizontal configuration and block off the cylinder's cross section. In turn, this leads to the added mass effect due to the water (7) trapped in the cylinder. The device remains in this state until it reaches point *b*, the topmost position in the cycle. Note that by the time *b* is reached, the horizontal plates (6) are near the bottom of the cylinder.

At *b*, the direction of motion is reversed, with the entire system accelerating down. Now the water pressure below the upper flaps is greater than above them, which forces the flaps to swing up and allows water to flow through the cylinder. The lower flaps (5) are still locked in the open state, so they cannot close, despite the increased water pressure from below. Therefore, no mass is added during the quarter cycle between *b* and *c*. Meanwhile, the sliding plates (6) are moving up relative to the cylinder.

At point *c* the downward motion continues, reaching the maximum vertical speed. As the plates (6) again pass through the midpoint (3) of the cylinder, they lock the upper flaps (4) in the open state and unlock the lower flaps (5), allowing them to close under increased water pressure from below. This again leads to the added mass effect, by trapping water (7) inside the cylinder. The system continues to move in this state until point *d*, by which time the sliding plates (6) have moved to the top of the cylinder.

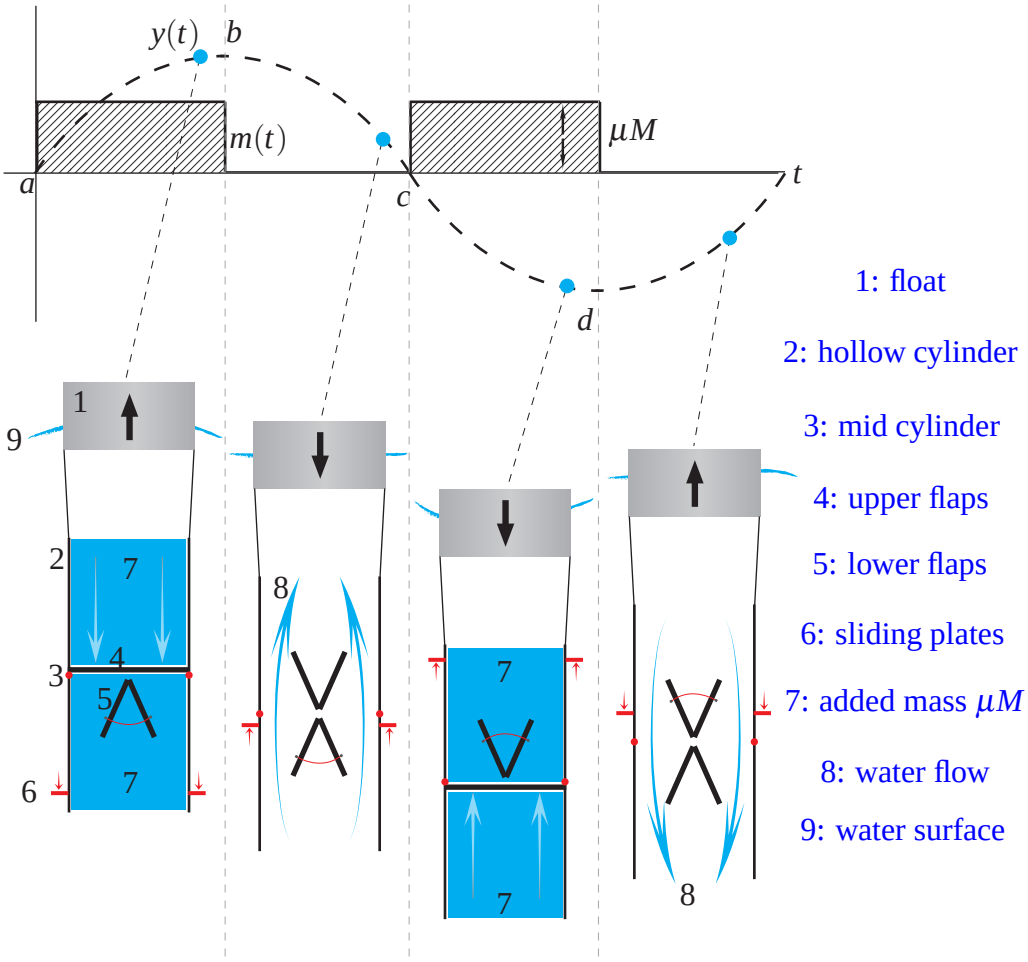

Fig. 7 Illustration of the operation of the water intake mechanism. An animation of the mechanism can be found at http://me.berkeley.edu/wec/water_intake_animation.html

At *d* the direction of motion is again reversed and the system starts to accelerate up. This forces the lower flaps (5) to open, and water flow through the cylinder is again established, resulting in no added mass. The horizontal plates (6) are now moving down relative to the cylinder, and when point *a* is reached in the next cycle, they pass through the midpoint (3), locking the lower flaps (5) open and unlocking the upper flaps (4) to close. The cycle then repeats. It should be noted that although the sliding horizontal plates (6) move up and down relative to the cylinder (2), their absolute position in the water remains approximately constant. Effectively, they act as inertial plates and remain stationary in the water.

2.3 Additional Comments on the Water Intake Mechanism

While the locking arrangement is helpful under ideal conditions, when the motion period becomes too short and both sets of flaps are installed, the mechanism may be left out. Since the flaps need time to close and open, it may take them about a quarter period to move between the two states, thus voiding the need to keep one set of flaps locked open. This was the observed case when we carried out our small-scale prototype tests in a tow tank facility. It was also discovered that when the motion period is short, a significant amount of interference occurs between the upper and lower flaps, preventing either pair from moving in the prescribed manner. However, we found that the water intake mechanism can still be functional with only the upper set of flaps installed, which greatly simplifies the physical design of the mechanism. The simplified scheme is discussed in Chapter 4.

Chapter 3

A Simple Model for the WEC

Before the water intake system from Chapter 2 could be constructed and tested experimentally, it makes sense to simulate it numerically and discover its performance potential. On the other hand, the ever changing geometry of the system make accurate modeling a very challenging task. While software tools such as WAMIT are capable of analyzing the static parameters of the system, dynamical models that incorporate hydrodynamic effects would need to be simulated using computational fluid dynamics (CFD) code. Such models would be complicated to develop and resource-intensive to run. Instead of going this route, we decided that the best course of action would be to create a very simple dynamics model of the WEC, leaving out explicit hydrodynamic effects, and determine (and improve) the performance of the system experimentally. The dynamics model, first discussed in [21] and revisited in [22] is presented below.

3.1 A One Degree of Freedom Hybrid System

The developed model of the WEC is a single degree-of-freedom (SDOF) damped, harmonically excited linear oscillator, whose mass m is modulated in time (cf. Fig. 8). The system features a square wave modulation in the mass parameter. An amount of water mass is added to the system for two of the quarter cycles, and no water mass is added during the other two quarter cycles. Referring to Fig. 7, the precise instants where water is added or released is governed by the instants when either the displacement y or velocity $\frac{dy}{dt}$ of the oscillator are zero. The effects of the ocean waves are modeled by an external harmonic excitation. Following the work of Salter et al. [10, 19, 27], we model the power takeoff as a damping element and this element is incorporated into the damping term in the model. The goal of the model is to examine how the power absorbed by the oscillator's PTO can be optimized using the state-dependent modulation of the mass. Due to the mass intake and release, we find that the model may also be conveniently described as a hybrid or switched linear system.

It is straightforward to show that the governing equations for the simple model are the

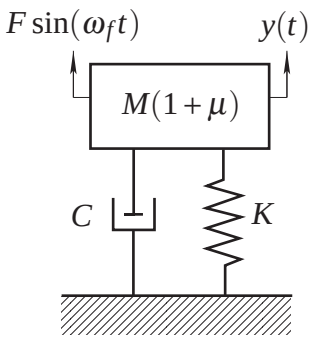

Fig. 8 Schematic for the single-degree-of-freedom linear oscillator

following system:

$$\begin{aligned} M(1+\mu)\frac{d^2y}{dt^2}+C\frac{dy}{dt}+Ky &= F\sin(\omega_f t), \qquad y\frac{dy}{dt}>0, \\ M\frac{d^2y}{dt^2}+C\frac{dy}{dt}+Ky &= F\sin(\omega_f t), \qquad y\frac{dy}{dt}<0. \end{aligned} \tag{3.1}$$

Here, y is the displacement of the mass, M is the default system mass, μM is the added mass, C is the damping coefficient (a sum of viscous damping from the water and external damping from the PTO), K is a spring constant of hydrodynamic origin, and F is the magnitude of the external excitation force (attributed to water waves) which is varying sinusoidally at a frequency ω_f. We refer to μ as the mass modulation parameter.

The system (3.1) is an example of a switched system where the switching conditions are state-dependent. The set of differential equations (3.1) needs to be supplemented by jump conditions at the locations where $y\frac{dy}{dt}=0$. These locations, which are referred to as the switching set, are along the $y=0$ and $\frac{dy}{dt}=0$ axes in the $y-\frac{dy}{dt}$ plane. For the simple model, we shall assume that $y(t)$ and $\frac{dy}{dt}$ are both continuous functions of time at the switching set. Continuity of $y(t)$ is easy to justify on the grounds that the motion of the oscillator is physically realistic. On the other hand, the continuity of $\frac{dy}{dt}$ assumes that the intake and release of the added mass μM does not result in impulsive loading.

3.1.1 Closed Form Solutions of the Hybrid System

We non-dimensionalize (3.1) by defining a time $\tau = t\sqrt{\frac{K}{M}}$ which is used to help transform (3.1) into

$$\begin{aligned} \ddot{x}+2\delta_1\dot{x}+\omega_{n_1}^2 x &= f_1\sin(\omega\tau), \qquad \dot{x}x>0, \\ \ddot{x}+2\delta_2\dot{x}+x &= f_2\sin(\omega\tau), \qquad \dot{x}x<0. \end{aligned} \tag{3.2}$$

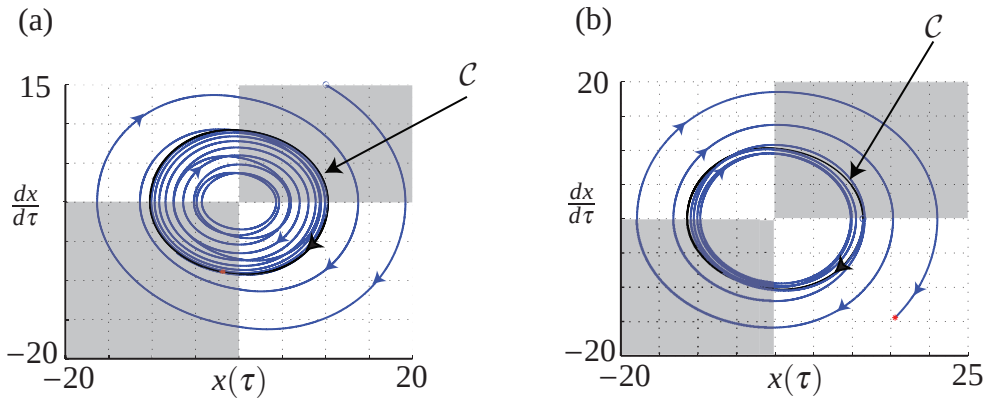

Fig. 9 Examples of limit cycles $\mathcal{C}$ and transient responses in their neighborhoods for the forced system (3.2) with $f = 1$, $\mu = 0.3$ and $\omega = 0.9$: (a) stable limit cycle ($\delta = 0.08$), and (b) unstable limit cycle ($\delta = 0.01$)

The $()'$ indicates a differentiation with respect to τ and the new parameters and fields are given by

$$\begin{aligned} x = \frac{y}{L}, \qquad f_1 &= \omega_{n_1}^2 f_2, \qquad \delta_1 = \frac{\delta_2}{(1+\mu)}, \qquad \omega_{n_1} = \sqrt{\frac{1}{1+\mu}}, \\ f_2 = f &= \frac{F}{KL}, \qquad \delta_2 = \delta = \frac{C}{2\sqrt{KM}}, \qquad \omega = \omega_f \sqrt{\frac{M}{K}}, \end{aligned} \tag{3.3}$$

where L is a suitable length scale[1]. The solutions to (3.2) are classical:

$$x = \begin{cases} x_1(\tau) \text{ when } \dot{x}x > 0, \\ x_2(\tau) \text{ when } \dot{x}x < 0. \end{cases} \tag{3.4}$$

Here,

$$\begin{aligned} x_1(\tau) &= e^{-\delta_1 \tau}\left(A_1 \cos(\omega_{d_1}\tau) + B_1 \sin(\omega_{d_1}\tau)\right) + X_1 \sin(\omega\tau - \phi_1), \\ x_2(\tau) &= e^{-\delta_2 \tau}\left(A_2 \cos(\omega_{d_2}\tau) + B_2 \sin(\omega_{d_2}\tau)\right) + X_2 \sin(\omega\tau - \phi_2), \end{aligned} \tag{3.5}$$

[1]For example, L could be chosen to be the maximum allowable displacement of the mass-spring-damper system

with

$$\begin{aligned} X_1 &= \frac{f_1}{\sqrt{\left(\omega_{n_1}^2-\omega^2\right)^2+\left(2\delta_1\omega\right)^2}}, \\ X_2 &= \frac{f_2}{\sqrt{\left(1-\omega^2\right)^2+\left(2\delta_2\omega\right)^2}}, \end{aligned} \tag{3.6}$$

and

$$\begin{aligned} \omega_{d_1} &= \omega_{n_1}\omega_{d_2}, \qquad \omega_{d_2}=\sqrt{1-\delta_2^2}, \\ \phi_1 &= \tan^{-1}\left(\frac{2\delta_1\omega}{\omega_{n_1}^2-\omega^2}\right), \qquad \phi_2=\tan^{-1}\left(\frac{2\delta_2\omega}{1-\omega^2}\right). \end{aligned} \tag{3.7}$$

For a given motion of the system, the constants A_α and B_α are prescribed by matching the solutions $x_1(\tau)$ and $x_2(\tau)$ at the appropriate switching boundaries $\mathcal{B}_i$, defined as

$$\begin{aligned} \mathcal{B}_1 &= \left\{(x,\dot{x})\,|x=0 \text{ and } \dot{x}>0\right\}, \\ \mathcal{B}_2 &= \left\{(x,\dot{x})\,|\dot{x}=0 \text{ and } x>0\right\}, \\ \mathcal{B}_3 &= \left\{(x,\dot{x})\,|x=0 \text{ and } \dot{x}<0\right\}, \\ \mathcal{B}_4 &= \left\{(x,\dot{x})\,|\dot{x}=0 \text{ and } x<0\right\}. \end{aligned}$$

It is tempting to assume that the solution to (3.2) will always be bounded if the input is bounded (i.e., BIBO stable). However, because we are dealing with a switched system, it is well-known that this is not necessarily the case (see [15, 17, 18]). Two representative examples of stable and unstable responses of the system are shown in Fig. 9. The limit cycles shown in these figures are the steady state response of the system. From numerical integrations of (3.2) we observe that for a fixed value of damping δ_2 if the mass modulation parameter μ is sufficiently small, then the response of the system will be BIBO stable. However, if μ is sufficiently large then the response will no longer have this property. Clearly, it is of interest to determine the regime where the system is BIBO stable. We now turn to this issue.

3.2 Bounded-Input-Bounded-Output Stability of the System

Of primary interest is to determine the parameters for BIBO stability of the switched system (3.2). For a given excitation $f_2\sin(\omega\tau)$, we observe that the system has a steady state response which is a limit cycle (cf. Fig. 9). We wish to determine the conditions for the stability of this limit cycle or equivalently the BIBO stability of the system.

Developing analytical criteria for the BIBO stability of the system is challenging. Several results are available and feature the construction of a Lyapunov function for a discrete-

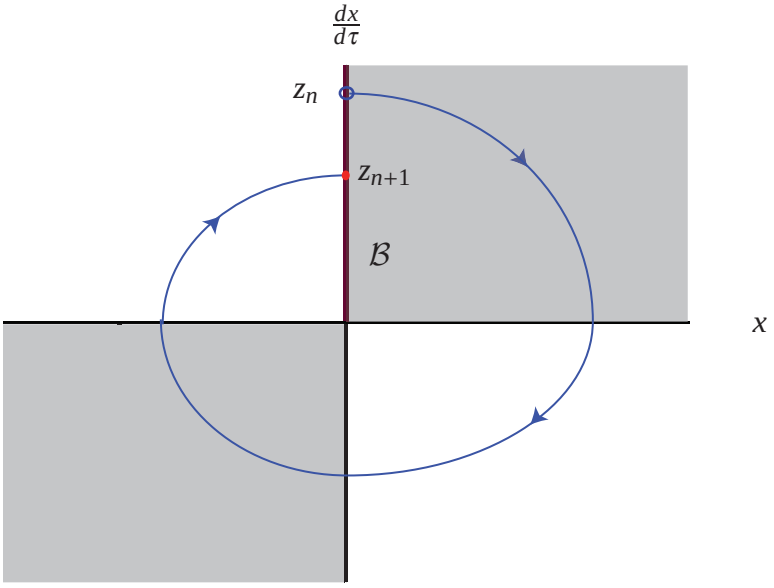

Fig. 10 Schematic of the phase flow of (3.8) and how it is used to construct the Poincaré map $\Phi : \mathcal{B} \to \mathcal{B}$

time equivalent system (see [12, 24]). In this section, we follow an alternative approach. First, we restrict attention to the unforced system and establish the stability criterion for its trivial equilibrium. To do this, we construct a one-dimensional Poincaré map. The resulting stability criteria are presented as a curve in the $\mu - \delta$ plane. We then examine the stability of the limit cycles observed in the forced system using an extensive series of numerical integrations. After these results are compiled, it becomes evident that the stability results for the unforced system provide a useful coarse estimate on the parameter regime for the BIBO of the forced system.

3.2.1 Stability of the Trivial Equilibrium

The unforced system is governed by the equations (from (3.2)):

$$\begin{aligned} \ddot{x} + 2\delta_1 \dot{x} + \omega_{n_1}^2 x = 0, \qquad & \dot{x}x > 0, \\ \ddot{x} + 2\delta_2 \dot{x} + x = 0, \qquad & \dot{x}x < 0, \end{aligned} \tag{3.8}$$

respectively. Clearly this system has a single trivial equilibrium. To examine the stability of the trivial equilibrium, we solve (3.8) over a time interval T. Referring to Fig. 10, it is easy to see that this allows us to define a Poincaré map Φ:

$$z_{n+1} = \Phi(z_n), \tag{3.9}$$

where

$$z_n = (0, \dot{x}(nT)) \in \mathcal{B}, \qquad n \in \mathbb{Z}^+. \tag{3.10}$$

The switching boundary $\mathcal{B}$ is

$$\mathcal{B} = \left\{ (x, \dot{x}) \,|x = 0 \text{ and } \dot{x} > 0 \right\}. \tag{3.11}$$

The time T is the time it takes for a solution of the differential equation to return to $\mathcal{B}$. For linear stability of the trivial equilibrium, we require the one-dimensional map Φ to be contractive.

After some work with the solutions of (3.8), we find that Φ is a simple linear mapping:

$$z_{n+1} = p^2 z_n. \tag{3.12}$$

The function p is defined by

$$p = \frac{1}{\omega_{n_1}} e^{-\delta_2 T_2} e^{-\delta_1 T_1} = e^{-\delta_2 T_2} e^{-\delta_1 T_1} \sqrt{1+\mu}, \tag{3.13}$$

where the times T_1 and T_2 are found by solving the transcendental equations

$$\begin{aligned} \frac{\delta_1}{\omega_{n_1}\omega_{d_1}} \tan(\omega_{d_1} T_1) &= 1, \\ \frac{\delta_2}{\omega_{d_2}} \tan(\omega_{d_2} T_2) &= -1. \end{aligned} \tag{3.14}$$

That is,

$$\begin{aligned} T_1 &= \frac{1}{\omega_{d_1}} \left(\arcsin\left(\sqrt{1 - \frac{\delta_1^2}{\omega_{n_1}^2}} \right) \right), \\ T_2 &= \frac{1}{\omega_{d_2}} \left(\pi - \arcsin\left(\sqrt{1 - \delta_2^2} \right) \right), \\ T &= 2T_1 + 2T_2. \end{aligned} \tag{3.15}$$

For stability, we require $|p| < 1$.

To determine the stability of the trivial equilibrium, we seek points where $|p| < 1$. This calculation leads to the stability region shown in Fig. 11. Clearly, there is a delicate balance here between mass modulation μ and damping δ_2. If the latter is sufficiently large, then stability will always be guaranteed. Otherwise, under perturbation, the trivial equilibrium will become unstable. In physical terms, if one adds and extracts too much mass then the oscillations will grow without bound if insufficient damping is present.

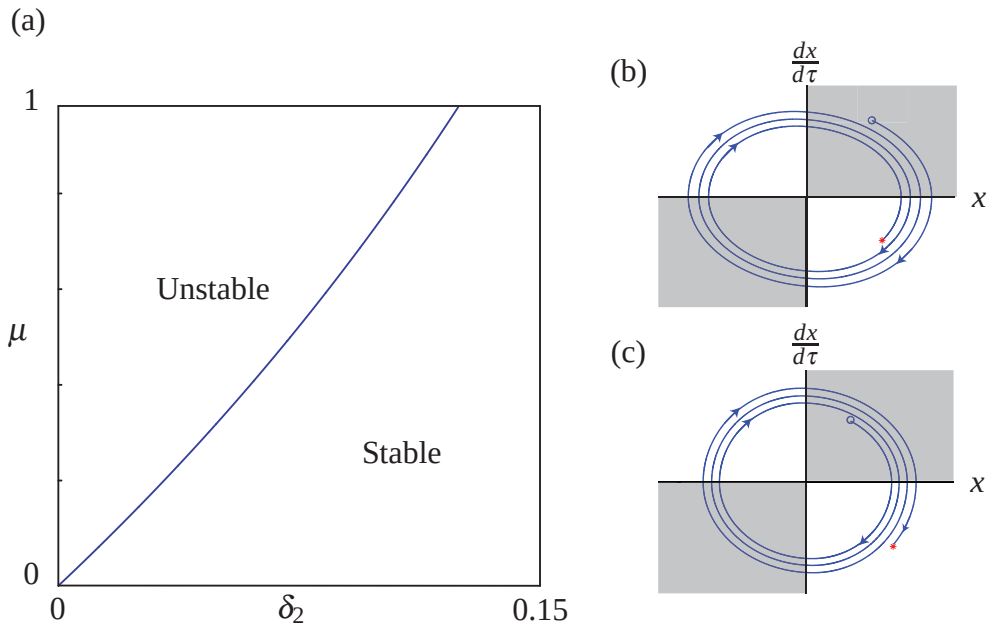

Fig. 11 Stability region for the trivial equilibrium of (3.8) is shown in (a). Representative phase portraits for stable and unstable cases of (3.8) are shown in (b) and (c), respectively

3.2.2 Numerical Investigation for BIBO Stability

When the system is harmonically excited (i.e., $f_{1,2}\sin(\omega\tau) \neq 0$), a limit cycle is observed. An explicit expression for $x(t) = x_L(t)$ corresponding to the limit cycle can be determined by piecewise matching of the solutions (3.5) to (3.2), and computing the time periods when the solution transits between elements of the switching set (which is defined by $x\dot{x} = 0$). The equations needed to determine $x_L(t)$ are nonlinear and must be solved numerically. An alternative method of finding the limit cycle is to numerically integrate (3.2) forwards (backwards) in time to find the stable (unstable) limit cycle. This is the approach we followed. One result that is evident from these simulations is that the $x_L(t)$ will contain contributions from the terms with frequencies $\omega_{d_{1,2}}$ in (3.5).

To examine the stability of the limit cycle, we numerically integrate (3.2) for various values of the excitation frequency ω. Of particular interest is the case $\omega = \omega_{\text{peak}}$, which corresponds to the excitation frequency which results in the largest displacement of the system. The value of ω_{peak} depends on μ and δ_2 and must be determined numerically. As can be seen from Fig. 12, the response of the system to this excitation frequency determines the BIBO stability regime. The stability criterion for the unforced case from Fig. 11 is also shown in Fig. 12. The proximity of the criteria for $f_2 = 0$ and $\omega = \omega_{\text{peak}}$ is remarkable. We now turn to examining limit cycles and other bounded oscillations in greater detail.

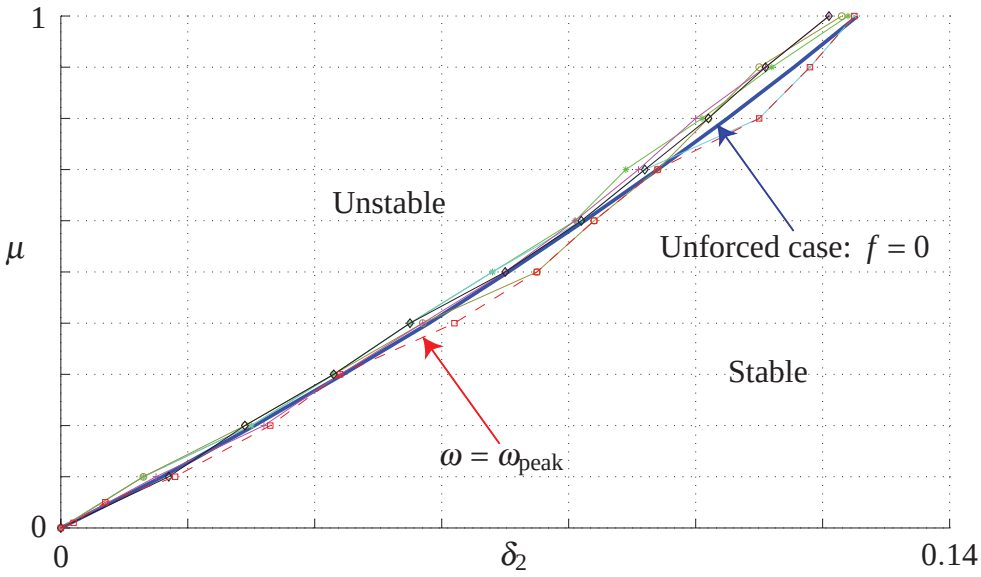

Fig. 12 BIBO stability regions for the forced system (3.2) for various excitation frequencies ω. The solid line is the stability criterion for the trivial equilibrium of the unforced system (cf. Fig. 11(a)). In this figure, $\square$: $\omega = \omega_{\text{peak}}$ $*$: $\omega = 0.8$, $\star$: $\omega = 0.85$, $\circ$: $\omega = 0.9$, $|$: $\omega = 0.95$, and $\diamond$: $\omega = 1.0$

3.3 Bounded Oscillatory Motions

Studying the stability and bifurcation of limit cycles and other bounded oscillations in hybrid systems is considered to be a challenging problem [8, 9, 11, 12, 14]. First, there is the inherent difficulty of finding closed-form expressions for the solutions to the equations governing these bounded motions. Secondly, the issue of determining the stability of the motion using either Floquet theory (see, e.g., [13]) or Lyapunov-based methods (see, e.g., [25]) can become tedious or intractable. We thus set a modest goal to catalogue the oscillatory motions of this relatively simple hybrid system, find a rich range of dynamical behaviors, and discuss the implications of these results on the energy harvesting capabilities of the WEC designed proposed in Chapter 2.

For the harmonically excited, damped linear oscillator in the absence of switching, it is easy to compute the single limit cycle and verify that it is globally attracting. Unfortunately, the situation with the switched system (3.2) is more complex. Among others, the typical steady-state analysis of seeking limit cycles by setting the terms multiplied by $e^{-\delta_\alpha \tau}$ to zero does not apply to (3.2). Through an extensive set of numerical integrations, we have been able to catalogue some of the bounded oscillatory motions of the switched system. We classify the bounded motions as stable and, in some instances, find that they are global attractors. In the event that the motions are closed orbits, we refer to them as limit cycles. The stability results in Section 3.2.1 can play a role in explaining these classifications.

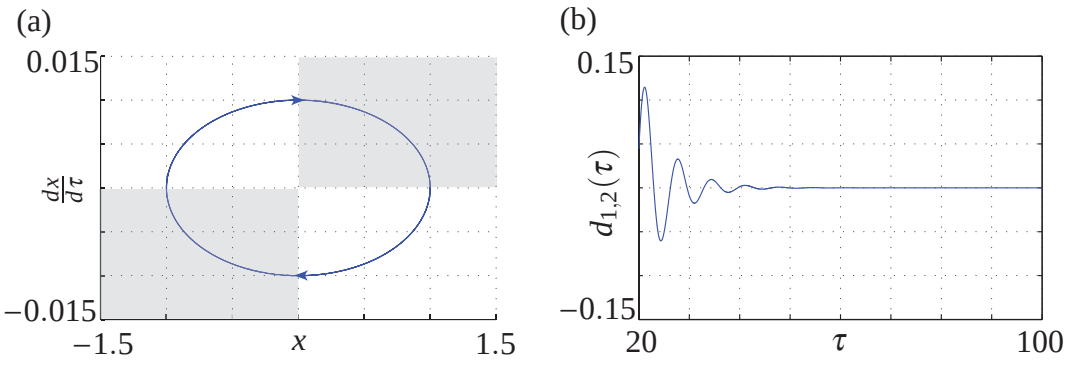

Fig. 13 An example of a low-frequency excitation of the oscillator: (a) the phase portrait of the terminal bounded oscillation; (b) the decay of the transient $d_\alpha(\tau) = x_\alpha(\tau) - X_\alpha \sin(\omega t - \phi_\alpha)$. For the results shown in this figure, $\delta = 0.2$, $\mu = 0.1$, $f = 1$, and $\omega = 0.01$

3.3.1 The Extremes of High-Frequency Excitation and Low-Frequency Excitation

The response of the oscillator to the regimes corresponding to low-frequency excitation where $\omega \ll 1$ and high frequency excitation where $\omega \gg 1$ can provide insight into classifying the behavior of the oscillator. Two examples of the bounded oscillations of the system for low- and high-excitation frequencies are shown in Figs. 13 and 14, respectively. The values of μ and δ chosen for this example are such that the unforced system would have a stable equilibrium.

In the low-frequency case, we find a limit cycle which is qualitatively similar to those we have observed for $\omega \leq 1$. The oscillation is bounded, and, after some initial transient behavior, the effects of $d_\alpha(\tau)$ appear to be negligible compared to $X_\alpha \sin(\omega\tau - \phi_\alpha)$. Despite this, finding a closed-form expression for the bounded oscillation has proven to be very difficult. The difficulty lies in solving the nonlinear equations for the transit times between the switching boundaries $\mathcal{B}_{1,2,3,4}$. As a result, we had to resort to numerical integrations of the equations of motion.

For the high-frequency case, $\omega \gg \omega_{n_\alpha}$ and it is easy to argue from (3.5) that $d_\alpha(\tau)$ is constant compared to $X_\alpha \sin(\omega\tau - \phi_\alpha)$ between switching intervals. As a result, the solution oscillates about $d_\alpha(\tau)$ with an amplitude of X. A typical example of this behavior is shown in Figure 14. In contrast to the low-frequency limit, it is difficult to argue that the bounded oscillation is a limit cycle. Another difference is that the limit cycle behavior for low ω transited the switching boundaries in the repeating sequence $\mathcal{B}_1$, $\mathcal{B}_2$, $\mathcal{B}_3$, $\mathcal{B}_4$, ... The corresponding sequence for the high-frequency case is erratic, and finding analytical expressions for the transit times is a daunting task.

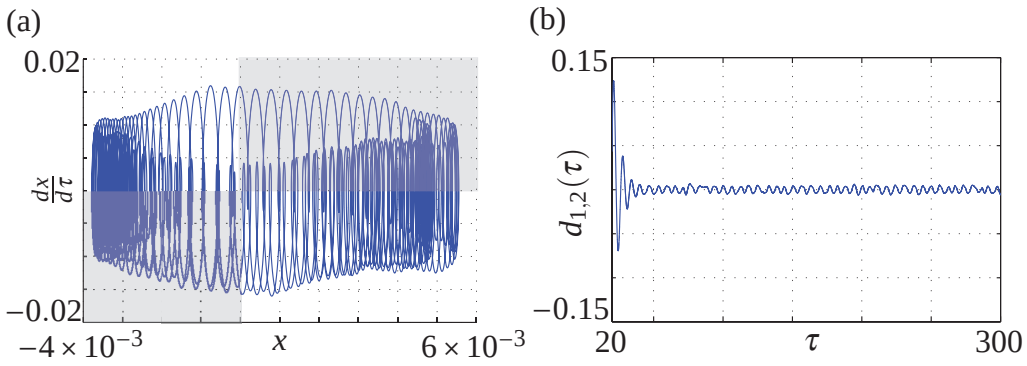

Fig. 14 An example of a high-frequency excitation of the oscillator: (a) the phase portrait of the terminal bounded oscillation; (b) the decay of the transient $x_\alpha(\tau) - X_\alpha \sin(\omega t - \phi_\alpha)$. For the results shown in this figure, $\delta = 0.2$, $\mu = 0.1$, $f = 1$, and $\omega = 100$

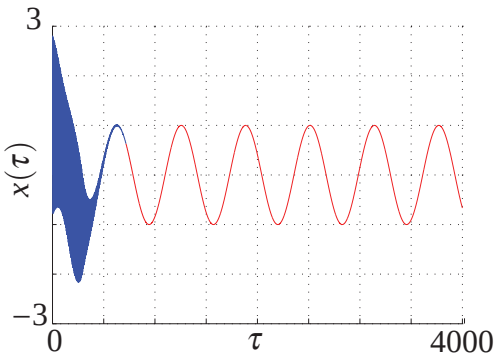

Fig. 15 Behavior of the $x(\tau)$ governed by (3.2) with $(x(0), \dot{x}(0)) = (0, 1.5)$, $\omega = 0.01$, $\delta = 0.014$, and $\mu = 0.1$. For these parameter values, $\omega_{d_1} = 0.953369$ and $\omega_{d_2} = 0.999902$

3.3.2 Global Attractors

An example of one of the interesting solutions to (3.2) can be seen in Fig. 15. Here, the transient behavior of $x(\tau)$ is dominated by higher frequency contributions from ω_{d_α}. The phase portrait corresponding to the solution shown in Figure 15 is displayed in Fig. 16(a), and it results in the bounded motion labeled $\mathcal{C}$ in the phase portrait. By selecting nearby initial conditions, we conclude that the limit cycle $\mathcal{C}$ is attractive. For the unforced system with the same values for μ and δ, it can be shown using the results of Section 3.2.1 - that the equilibrium is unstable: $\mu > \mu_e(\delta)$. With this in mind, we find that choosing an initial condition such that $d_\alpha(\tau)$ dominates $X_\alpha \sin(\omega\tau - \phi_\alpha)$ produces an oscillation that becomes unbounded. Such a solution is shown in Fig. 16(b). Thus, the limit cycle, which is labeled $\mathcal{C}$ in Fig. 16, is not globally attracting.

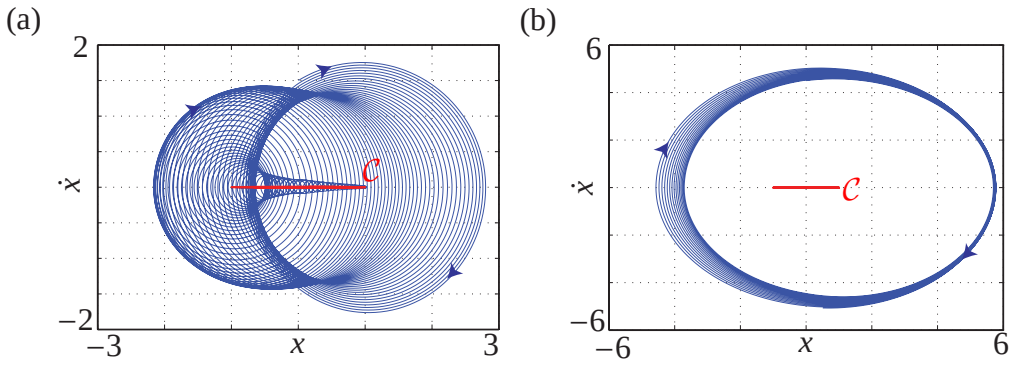

Fig. 16 Phase portraits of the solution to (3.2) with $\omega = 0.01$, $\delta = 0.014$, and $\mu = 0.1$, and the initial conditions (a) $(x(0),\dot{x}(0)) = (0,1.5)$ and (b) $(x(0),\dot{x}(0)) = (0,4.5)$

To distinguish the subset of global attractors from the set of stable bounded motions, we performed an extensive set of numerical integrations of the hybrid system for discrete values of μ, δ, and ω. A summary of some of our results is shown in Fig. 17. To construct Fig. 17(a), several initial conditions far from the bounded oscillation of interest were chosen and their long-term behaviors investigated. This yielded information on the global stability of the bounded oscillation associated with the parameter values μ, ω, and δ. For given ω and δ, the corresponding value of μ beyond which the bounded motion ceases to be a global attractor is labeled μ_G. The difference between this value of μ and the corresponding value of $\mu_e = \mu(\delta)$ where the unforced equilibrium becomes unstable is shown in Fig. 17(a). The corresponding critical value of μ where the bounded oscillatory motion is stable but not globally attracting is denoted by μ_L and results for $\mu_L - \mu_e$ are shown in Fig. 17(b).[2]

In Fig. 17(b), the results for $\omega = 0.01$ and $\omega = 0.1$ are not shown because $\mu_L - \mu_e$ for these cases are orders of magnitude larger than the results for $\omega = 1,5$. Instead, the values of μ_L for these frequencies are shown separately in Fig. 18. It is interesting to note how the stability results for the trivial equilibrium of the unforced system provides a conservative bound for the stability of limit cycles associated with the forced system. Furthermore, the figure illustrates how low-frequency excitations can be used to generate stable limit cycles in the neighborhood of the point $(0,0)$ which would be unstable if the amplitude of the external excitation were 0 (i.e., $f = 0$).

For a given set of parameter values of ω and δ, we found that $\mu_L > \mu_G$. A representative set of results are shown in Fig. 19 for $\omega = 1$. In general we found that $\mu_G < \mu_e$ for a given pair of ω and δ. This finding is easy to explain. Far from the origin of the forced system, the dynamics are dominated by the unforced response. If the origin is stable, then the trajectories in this far field are attracted to the origin and this enables the possibility of a globally attracting state.

[2]The results in Fig. 17 were obtained to an accuracy of 0.0001 for $|\mu_G - \mu_e|$ and $|\mu_L - \mu_e|$

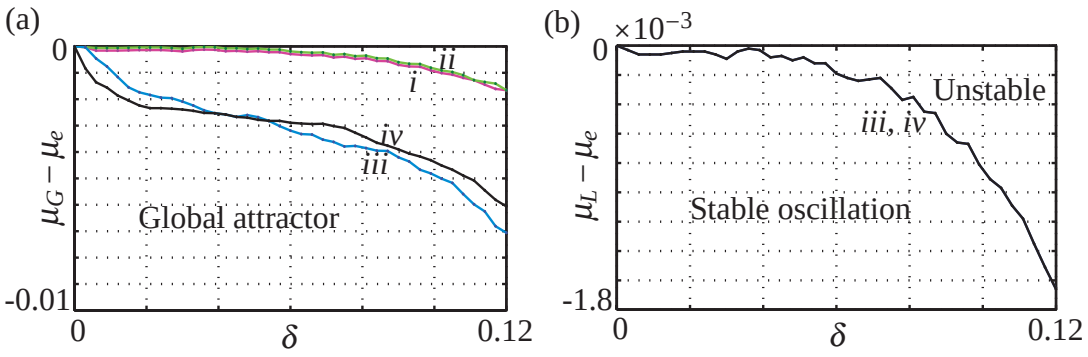

Fig. 17 The $\mu_G - \mu_e$ and $\mu_L - \mu_e$ values as functions of the damping $\delta = \delta_2$ for a range of frequencies for a range of values of ω. (a) Global asymptotic stability of the bounded motion and (b) local asymptotic stability of the bounded motion. In this figure, *i* denotes $\omega = 0.01$, *ii* denotes $\omega = 0.1$, *iii* denotes $\omega = 1.0$, and *iv* denotes $\omega = 5.0$

3.3.3 Amplitudes of Bounded Motions

One characterization of the dynamics of the system alluded to in Section 3.3.2 is to compute the amplitude of the bounded motion that the system exhibits after the initial transients have decayed. This numerical computation is performed by simulating the system for a sufficiently long time to ascertain if it asymptotes to a bounded oscillation.[3] Then, the maximum positive value of $x(\tau)$ during the bounded oscillation is defined as the magnitude x_{mag}. These results are compiled in Fig. 20. In addition, the results for the non-switched system ($\mu = 0$) are also presented for the purpose of comparison. Bounded oscillations do not exist for all values of μ, δ, and ω. In particular, given ω and μ, we found that for sufficiently low values of δ the solutions to the equations of motion became unbounded. These regions are denoted by U in Fig. 20.

For the results shown in Fig. 20(a-c), the bounded oscillations correspond to limit cycles. However, as ω increases, the bounded oscillations become more complex. Thus, in Fig. 20(d), the dashed lines indicate the region where the oscillation is bounded but is not a limit cycle. Some representative examples of solutions for the case $\mu = 0.5$ and $\omega = 2.0$ were shown earlier in Fig. 15. An example of an unstable limit cycle when the damping is low ($\delta = 0.05$) was shown in Fig. 15(d). With regard to the results displayed in Fig. 20(e), where ω is far from any of the resonant frequencies $\omega_{r_{1,2}}$, the results show the magnitude of the bounded oscillations but none of these oscillations are limit cycles.

[3]Recall, that when the oscillation results in a closed orbit, such as those shown in Fig. 22(a), as opposed to the oscillation of the form shown in Fig. 14, then we refer to it as a limit cycle.

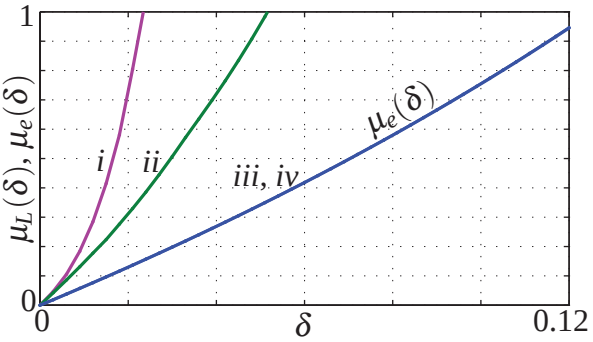

Fig. 18 The μ_L values as functions of the damping $\delta = \delta_2$ for four specific values of the frequency ω. The function $\mu_e(\delta)$ is also shown for comparison (cf. Figure 11). In this figure, *i* denotes $\omega = 0.01$, *ii* denotes $\omega = 0.1$, *iii* denotes $\omega = 1.0$, and *iv* denotes $\omega = 5.0$

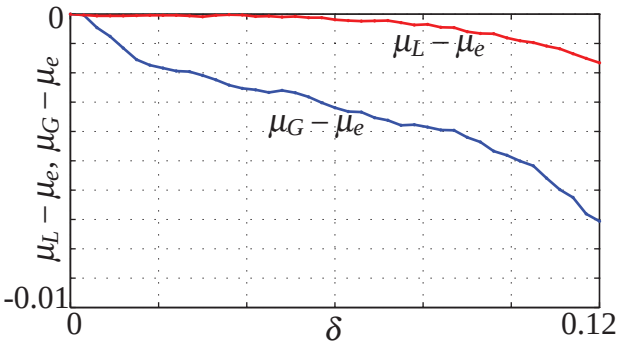

Fig. 19 The $\mu_L - \mu_e(\delta)$ and $\mu_G - \mu_e(\delta)$ values as functions of the damping $\delta = \delta_2$ for the frequency $\omega = 1$

3.3.4 Unstable States

To further catalog the behavior of the hybrid system, we next examined the magnitude of bounded oscillatory motions for a wide range of values of μ, δ, and ω. The results of this extensive set of numerical integrations are shown in Fig. 20. As evidenced from this figure, for several parameter regimes no bounded motions were found.

To illustrate the dynamic responses examined while compiling the results in Fig. 20, consider the case where $\omega = 2$, $f = 1$, and $\mu = 0.5$. The variation of the amplitude of the bounded oscillations with changing damping for this case can be inferred from Fig. 20(d). As shown in Fig. 21(a), when the damping is large, the system has a globally attracting bounded motion which we classify as a limit cycle. As the damping gets smaller, we were unable to characterize the motion as a closed limit cycle, but were able to conclude that it is a bounded global attractor (see Fig. 21(b,c)). When the damping is insufficient, no stable bounded motion could be found and instead, by backward integration, we found the unstable limit cycle a shown in Fig. 21(d).

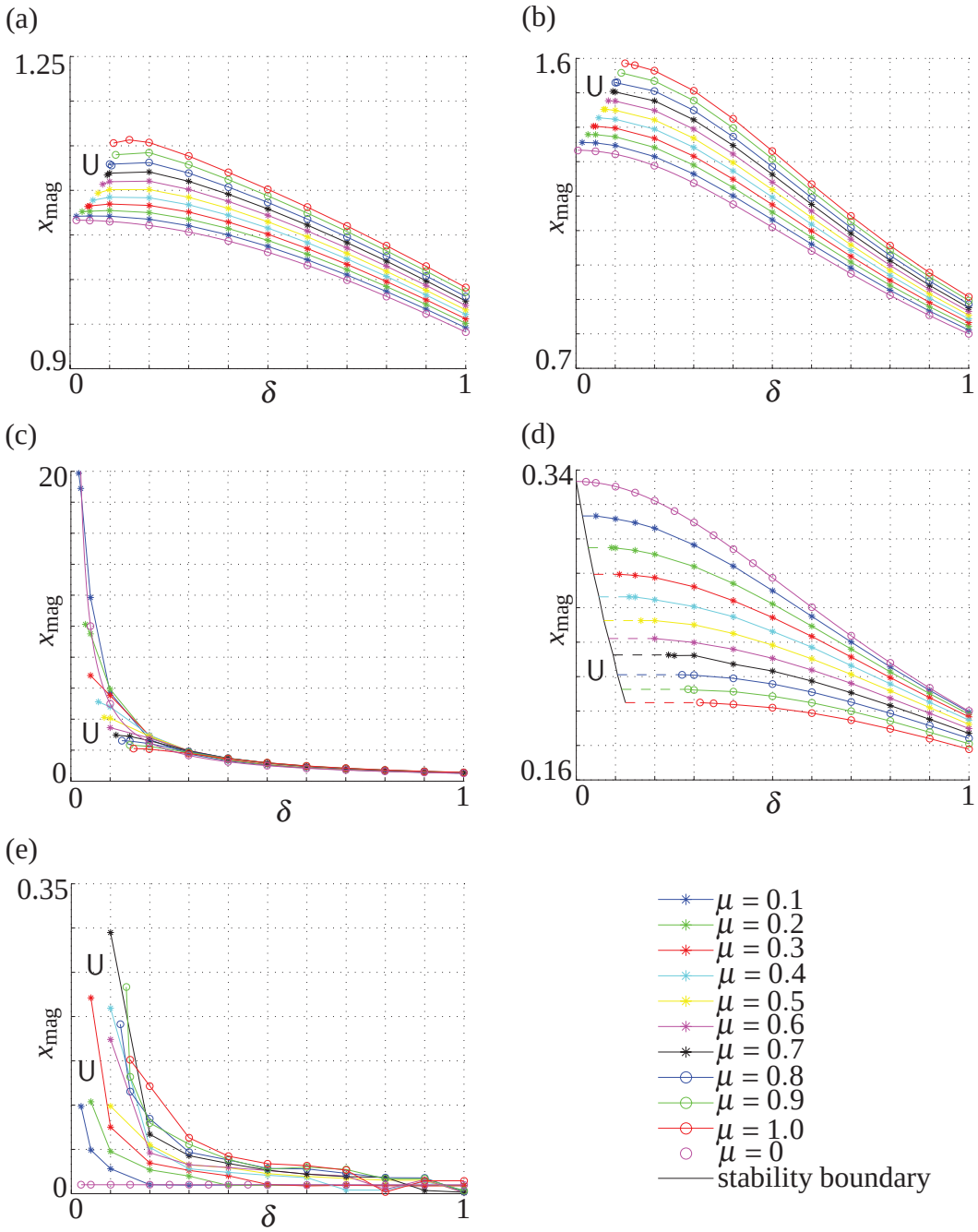

Fig. 20 Amplitude of bounded oscillations as a function of damping δ and forcing frequency ω for different values of μ. For $\mu = 0$, the analytical solution is plotted together with numerical results. (a) $\omega = 0.25$; (b) $\omega = 0.5$; (c) $\omega = 1$; (d) $\omega = 2.0$; and (e) $\omega = 10$. The label U denotes regions in the parameter space where no bounded oscillations were found

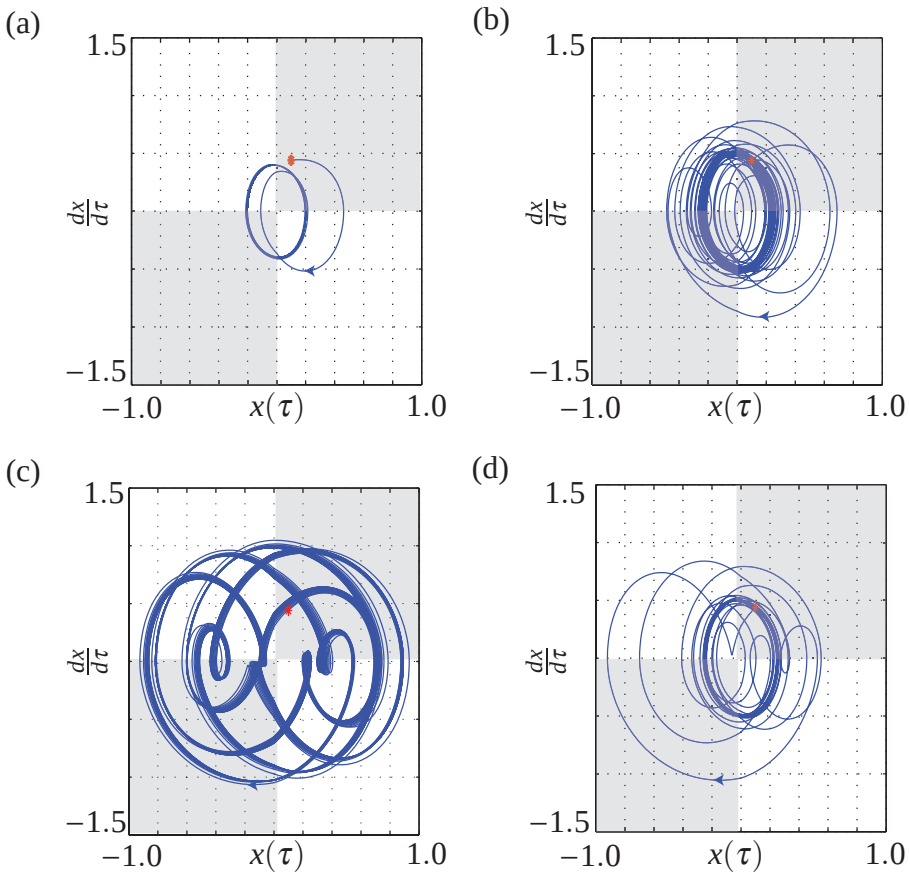

Fig. 21 Oscillations of the hybrid system for various values of damping δ: (a) $\delta = 0.9$, (b) $\delta = 0.2$, (c) $\delta = 0.1$, and (d) $\delta = 0.05$. For the results shown in this figure, $\mu = 0.5$, $f = 1$, and $\omega = 2.0$. The $\cdot$ denotes the initial condition $(x(\tau_0 = 0), \dot{x}(\tau_0 = 0)) = (0.1, 0.4405)$. The limit cycle in (d) is unstable

3.3.5 *A Coarse Estimate*

For low-frequency excitation where $\omega \ll 1$ we observe from the numerical simulations that a limit cycle is present (see Figs. 13 and 16). Further, from the results shown in Fig.18 we can conclude that the limit cycle is stable (although it is not necessarily a global attractor), even though μ may be greater than $\mu_e(\delta)$ for the given parameter pair (μ, δ) of interest. We now use these observations to develop a coarse estimate for the limiting low-frequency behavior when f, μ, and δ are $O(1)$ and $\omega = \varepsilon\omega_0$, where $\varepsilon \ll 1$.

With the help of (3.5), and (3.6), it can be shown that

$$X_2 = X_1 + O(\varepsilon^2), \qquad X_1 = f + O(\varepsilon^2), \tag{3.16}$$

and

$$\phi_1 = 2\varepsilon\delta\omega_0 + O(\varepsilon^3), \qquad \phi_2 = 2\varepsilon\delta\omega_0 + O(\varepsilon^3). \tag{3.17}$$

If the initial conditions at $\tau = \tau_0$ are chosen so that $d_\alpha(\tau_0)$ is small, then $d_\alpha(\tau)$ will decay and $x(\tau)$ will be dominated by $X_\alpha \sin(\omega\tau)$. In this case, we find an asymptotic estimate for the limit cycle as $\varepsilon \to 0$ is an ellipse in the phase plane:

$$\frac{x^2}{f^2} + \frac{\dot{x}^2}{\omega^2 f^2} = 1. \tag{3.18}$$

In simulations of the low-frequency case, such as those shown in Fig. 13,[4] we typically found that the transient behavior can be very complex with multiple passages of the trajectory through the switching boundaries. However, eventually the limiting state of the trajectory is an ellipse in the phase plane.

3.3.6 *Energetic Considerations*

The state-dependent mass modulation that is a central feature of the hybrid system was motivated by the desire to increase the energy harvesting capabilities of a wave energy converter. On a related note, it is interesting to examine the temporal behavior of the total energy of the oscillator. To this end, the total energy E of the oscillator has the representations

$$\begin{aligned} E = E_1 &= \frac{M(1+\mu)}{2}\left(\frac{dy}{dt}\right)^2 + \frac{K}{2}y^2, \qquad y\frac{dy}{dt} > 0, \\ E = E_2 &= \frac{M}{2}\left(\frac{dy}{dt}\right)^2 + \frac{K}{2}y^2, \qquad y\frac{dy}{dt} < 0. \end{aligned} \tag{3.19}$$

[4] See also the limit cycle shown in Figs. 15 and 16

With the help of (3.3), we find expressions for the dimensionless energy e of the oscillator:

$$\begin{aligned} e = e_1 &= \frac{1+\mu}{2}\dot{x}^2 + \frac{\omega_{n_2}^2}{2}x^2, \qquad \dot{x}x > 0, \\ e = e_2 &= \frac{1}{2}\dot{x}^2 + \frac{\omega_{n_2}^2}{2}x^2, \qquad \dot{x}x < 0. \end{aligned} \tag{3.20}$$

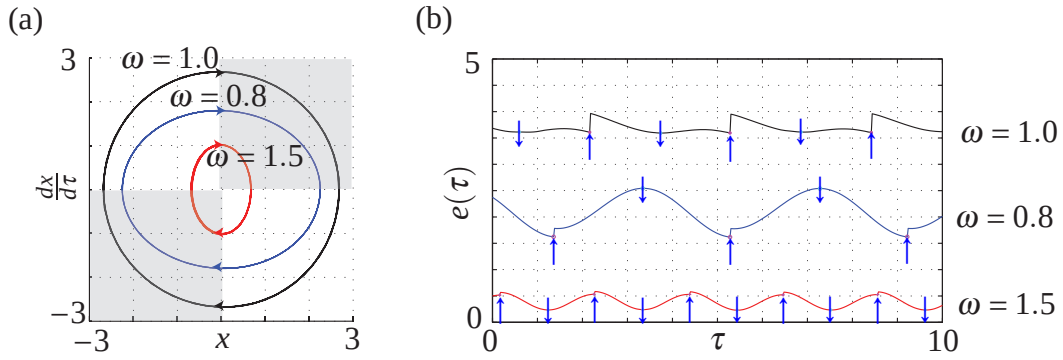

Fig. 22 Samples of (a) bounded oscillations and (b) their associated energy e. For the results shown in this figure, $\delta = 0.2$, $\mu = 0.1$, and $f = 1$, and three values of ω have been used: $\omega = 0.8$, $\omega = 1.0$, and $\omega = 1.5$. In (b), the $\uparrow$ indicates the instances where the mass jumps from M to $M(1+\mu)$, while the $\downarrow$ indicates the instances where the mass decreases from $M(1+\mu)$ to M

As can be seen from Fig. 22, bounded oscillatory motions feature jumps in the energy e at the pair of switching boundaries $\mathcal{B}_1$ and $\mathcal{B}_3$ on the $x = 0$ axis where the mass changes from M to $M(1+\mu)$. We also observe from this figure that, even for moderate levels of damping, the average value of the energy e of the oscillator increases dramatically as ω approaches the resonance frequency. The exact cut-off frequency ω where the non-switched system (i.e., where $\mu = 0$) has a lower energy than the switched system depends on the value of δ. In the interests of brevity, we do not present these results here, however generally we found that e will have lower (higher) values than the switched system when $\omega \leq 1$ ($\omega \gg 1$).

3.4 The Efficacy of Mass Modulation for Energy Harvesting

Of crucial interest is the amount of energy harvested by the oscillator compared to the energy which is incident on the oscillator due to the forcing $f\sin(\omega_f t)$. To compute the harvested energy it suffices to calculate the average power per cycle of the external forcing that the system can harness. Here, the harnessed power [7, 10, 19, 27, 29] is taken to be

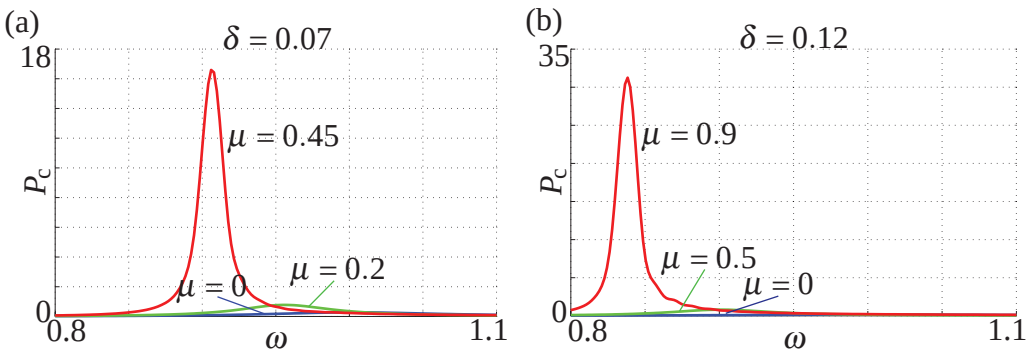

Fig. 23 Average power per cycle P_c as a function of driving frequency ω for selected values of damping factor $\delta = \frac{C}{2\sqrt{KM}}$ as indicated on the figure. Maximum power per cycle for each case is shown in Table 1

proportional to the damping coefficient $\delta = \delta_2 = \frac{C}{2\sqrt{KM}}$ and the velocity squared.[5] That is, the average power harvested is

$$P_{\text{avg}} = \frac{\delta}{T}\int_0^T \dot{x}^2 d\tau. \tag{3.21}$$

The average power per cycle is then given by dividing P_{avg} by the number of cycles during this time interval. First, we note that

$$T_{\text{cycle}} = \frac{2\pi}{\omega}, \qquad \omega = \omega_f\sqrt{\frac{M}{K}}. \tag{3.22}$$

Then, the average power per cycle P_c is

$$P_c = \frac{P_{\text{avg}}}{T_{\text{cycle}}} = \frac{\delta}{T\cdot T_{\text{cycle}}}\int_0^T \dot{x}^2 d\tau. \tag{3.23}$$

Simulating the system for a range of frequencies and computing P_c, gives the results shown in Fig. 23. When computing these results, values of μ and δ corresponding to BIBO stability of the system were selected.

The results shown in Fig. 23 were obtained using μ values corresponding to 0%, 20%, 45%, 50% and 95% of the total mass M, respectively. For higher values of the mass modulation parameter μ the plots show a marked increase in power produced by the excited system, compared to the regular case (i.e., the case $\mu = 0$ shown in Fig. 23(a)). The maximum power per cycle $P_{c_{\max}}$ values for each of the cases presented in Fig. 23 are given in Table 1. These results demonstrate that the mass modulation can significantly improve the

[5]This damping coefficient δ is the sum of the damping provided by the PTO and the hydrodynamic damping. We tacitly assume that the latter is constant in our analyses, and assume that the variation of δ can be achieved by altering the parameters of the PTO

Table 1 Maximum power per cycle $P_{c_{max}}$ for various values of damping factor $\delta = \frac{C}{2\sqrt{KM}}$ and mass modulation parameter μ, and the associated forcing frequency ω at which maximum power occurs. All presented combinations of δ and μ result in a stable system

$P_{c_{max}}$	$\mu = 0$	$\mu = 0.2$	$\mu = 0.45$	$\mu = 0.50$	$\mu = 0.90$
$\delta = 0.07$	0.27	0.78	16.6	-	-
ω @ $P_{c_{max}}$	1.001	0.956	0.906	-	-
$\delta = 0.12$	0.16	-	-	0.81	31.3
ω @ $P_{c_{max}}$	1.001	-	-	0.900	0.838

energy harvesting capabilities of the oscillator. It should also be noted that in contrast to a regular system where $\mu = 0$, the power peak for the mass modulated system lies to the left of the $\omega = 1$ line. Since $\omega = \frac{\omega_f}{\sqrt{K/M}}$ does not take into account the mass modulation μ term (which would lower the value of the resonant frequency), effectively $\omega = 1$ lies above the resonant frequency for the system with the novel excitation scheme.

3.5 The Maximum Power that Can Be Harnessed When the Amplitude of Motion is Limited

Unfortunately, the dramatic increase in absorbed power happens primarily at low values of damping, and correspondingly high amplitudes of oscillation. In practice, this would not be achievable, as there would inevitably exist a number of restrictions (such as stroking, slamming and force restrictions) on the maximum allowable response amplitude. To explore this issue further, we now examine the power which can be harvested if the response amplitude of the system is restricted.

In this section, we discuss an analytical expression for the optimum damping coefficient δ as a function of driving frequency ω which maximizes P_c at every ω. We start our analysis with the case where there is no mass modulation (i.e., $\mu = 0$), and then supplement these results with numerically obtained values of the damping coefficients that maximize the harvested power for the cases where the mass is modulated using the novel excitation scheme.

For practical reasons, the system's response amplitude often needs to be limited to some

maximum value $X_{\max}$. Using this value in $(3.6)_2$ and solving for δ yields

$$\delta_{\min} = \frac{1}{2\omega}\sqrt{f^2 - X_{\max}^2(1-\omega^2)^2}. \tag{3.24}$$

This expression gives the lower bound on the value of δ necessary to keep the response amplitude at or below $X_{\max}$. Yet, for $\omega \le \sqrt{1-f/X_{\max}}$ or $\omega \ge \sqrt{1+f/X_{\max}}$, it is evident that $\delta_{\min}$ given by (3.24) has no real component, meaning that the harnessed power in (3.23) is zero. This also means that for these frequency ranges, the system would not be able to oscillate at an amplitude of $X_{\max}$ while absorbing power from the damper. Thus, we need to find a value of δ that will produce the maximum power at each driving frequency ω, regardless of amplitude constraints. To do this, we use $(3.6)_2$ to establish an expression for $\dot{x}^2$ in (3.23) and then differentiate the resulting integral with respect to δ. This is equivalent to maximizing the function S as a function of δ where

$$S(\delta) = \frac{f^2\omega^2\delta}{(1-\omega^2)^2 + 4\delta^2\omega^2}. \tag{3.25}$$

Solving for the values of δ where $\frac{\partial S}{\partial \delta} = 0$, we find two values depending on the value of ω:

$$\delta_{\mathrm{A}}^* = \frac{1-\omega^2}{2\omega}, \qquad \delta_{\mathrm{B}}^* = \frac{\omega^2-1}{2\omega}. \tag{3.26}$$

Examining $\frac{\partial^2 S}{\partial \delta^2}\left(\delta = \delta_{\mathrm{A,B}}^*\right)$ and evaluating it at $\delta_{\mathrm{A,B}}^*$ we find that it is negative. Thus $\delta_{\mathrm{A,B}}^*$ yield maximum values of harvested power. Clearly, $\delta_{\mathrm{A,B}}^* \to 0$ as $\omega \to 1$, so in the vicinity of the resonant frequency these values are not feasible. Therefore, instead of looking at a single expression for optimal damping, we need to simultaneously take into account (3.24) and (3.26). Fig. 24 shows a plot of $\delta_{\mathrm{A,B}}^*$ and $\delta_{\min}$ as functions of ω.

We note that for $\omega < \omega_{\mathrm{A}}^*$, $\delta_{\mathrm{A}}^* > \delta_{\min}$. Since δ_{A}^* is set to maximize harnessed power without regard to amplitude limits, and it exceeds the minimum value of damping needed to keep the response amplitude bounded, this is the value of the damping coefficient that should be used in this frequency range. Likewise, for $\omega > \omega_{\mathrm{B}}^*$, $\delta_{\mathrm{B}}^* > \delta_{\min}$, so δ_{B}^* should be set as the damping coefficient. But in the range $\omega_{\mathrm{A}}^* \le \omega \le \omega_{\mathrm{B}}^*$, $\delta_{\min}$ is the lowest damping value at which $X_{\max}$ is not exceeded. Hence $\delta_{\min}$ is the damping setting of choice in this intermediate frequency range. Equating (3.24) and $(3.26)_1$, we can solve for the values of ω_{A}^* and ω_{B}^*:

$$\omega_{\mathrm{A}}^* = \sqrt{1 - \frac{f}{\sqrt{2}X_{\max}}}, \qquad \omega_{\mathrm{B}}^* = \sqrt{1 + \frac{f}{\sqrt{2}X_{\max}}}. \tag{3.27}$$

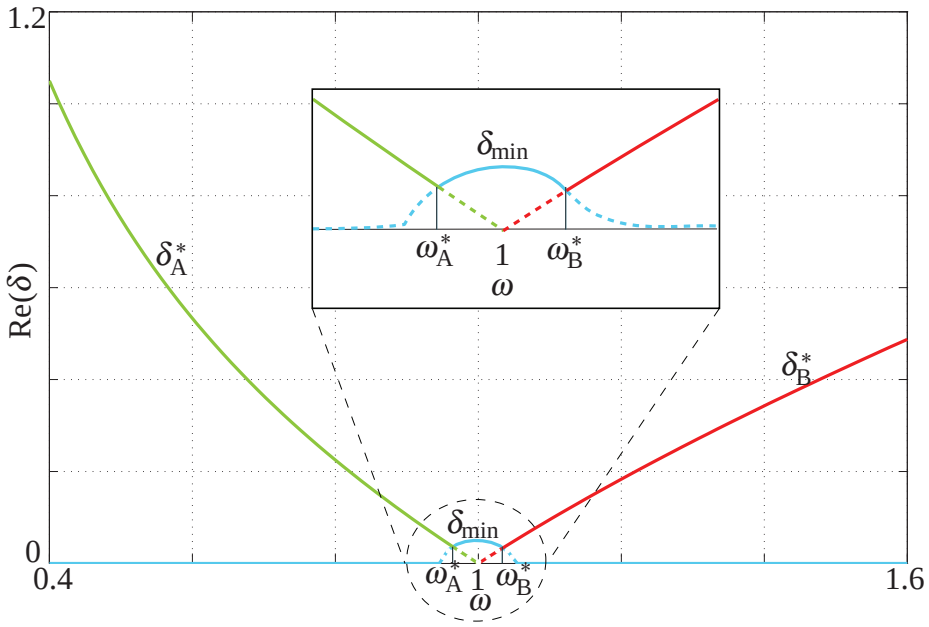

Fig. 24 Real positive parts of damping factors given by (3.24) and (3.26) as functions of driving frequency ω. The plot for optimal δ is shown as a solid line. $\delta_{\min}$ was computed using $X_{\max} = 1$ and $f = 0.1$. Note that the peak for $\delta_{\min}$ occurs slightly below $\omega = 1$. This is because the peak response amplitude (but not power, as per [29]) for a damped system occurs at $\omega_p = \omega_n\sqrt{1-2\delta^2}$, where ω_n is the undamped natural frequency (which is equivalent to $\omega = 1$ in our model)

Hence, the optimal damping coefficient is given by

$$\delta_{\text{opt}} = \begin{cases} \dfrac{1-\omega^2}{2\omega}, & 0 \le \omega < \omega_{\text{A}}^* \\ \dfrac{1}{2\omega X_{\max}}\sqrt{f^2 - X_{\max}^2(1-\omega^2)^2}, & \omega_{\text{A}}^* \le \omega < \omega_{\text{B}}^* \\ \dfrac{\omega^2-1}{2\omega}, & \omega_{\text{B}}^* \le \omega. \end{cases} \tag{3.28}$$

As an illustration, Fig. 25 shows the power harvested per cycle and maximum response amplitude as functions of frequency ω when δ_{opt} is used. Note that the peak in power occurs at a frequency ω_m to the right of $\omega = 1$. This is due to the fact that while response amplitude is capped at $X_{\max}$ for both frequencies, the value of the velocity $\dot{x}$ is higher at ω_m. Indeed, the ratio of peak power to that at $\omega = 1$ is proportional to the ratio of these two frequencies.

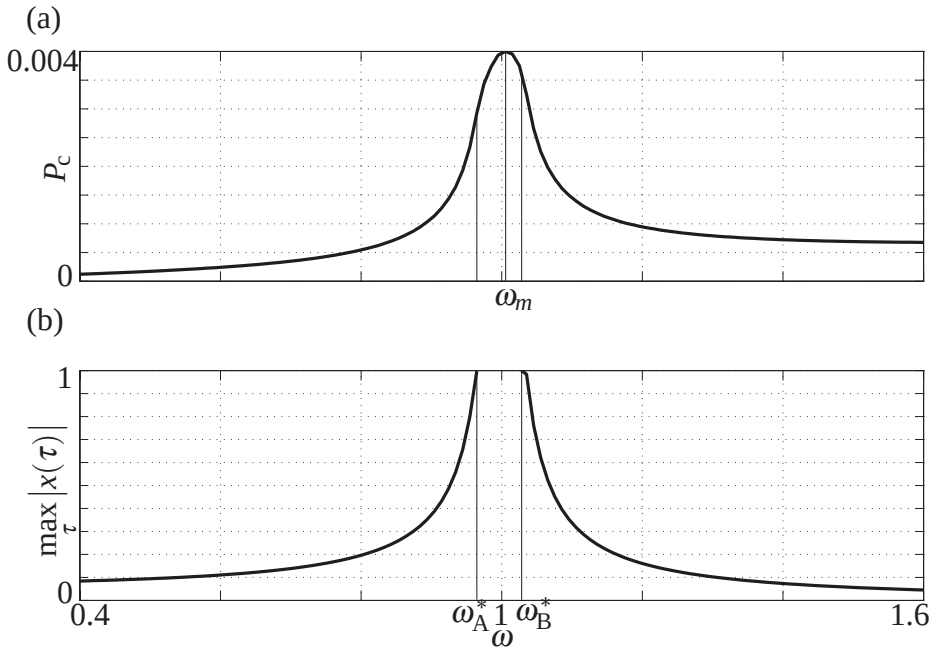

Fig. 25 (a) Average power harvested per cycle P_c and (b) response amplitude as functions of driving frequency ω using the damping values given by (3.28). Simulations were performed using $f = 0.1$ and $X_{\max} = 1$

Next, we perform a set of simulations to determine optimal damping values at each excitation frequency ω that maximize harnessed power per cycle. Unlike the cases presented in Fig. 23, we impose an amplitude constraint of $X_{\max} = 1$ at all frequencies. The

Table 2 Maximum power per cycle $P_{c_{max}}$ and the associated optimal values of damping δ_{opt} for plots shown in Fig. 26

	$\mu = 0$	$\mu = 0.1$	$\mu = 0.2$	$\mu = 0.3$
$P_{c_{max}}$	0.004	0.005	0.0057	0.0065
ω at $P_{c_{max}}$	1.005	0.9849	0.9647	0.9445
δ_{opt} at $P_{c_{max}}$	0.0495	0.0659	0.0828	0.0975

simulation program then sweeps through a range of damping values δ at each frequency, computes the power and maximum amplitude, and selects the damping value at which P_c is the largest while $\max_{\tau} |x(\tau)| \leq 1$. The results are presented in Fig. 26 for μ values of 0, 0.1, 0.2 and 0.3, while maximum power and optimal damping values are shown in Table 2. An inspection of Fig. 26(a) reveals that when the amplitude is restricted, mass modulation no longer provides the large improvements in harvested power that Fig. 23 showed. The improvements in maximum harnessed power at μ values of 0.1, 0.2 and 0.3 are 25%, 42.5% and 62.5%, respectively. The gains would be larger if X_{max} were larger.

Looking at Fig. 26(b), we observe that for all cases where mass modulation is present, the maximum response amplitude hovers around the $X_{max} = 1$ mark. This means that amplitude constraints take precedence over power maximization. It is of interest to compare this to the case of the constant mass system which is shown in Fig. 26(a)–(c) and labelled $\mu = 0$. For this case, the maximum amplitude drops off on both sides of $\omega = 1$ to maximize power, as given by (3.26). Finally, Fig. 26(c) shows that there is little variation in the optimal damping coefficients for the cases where $\mu \neq 0$. Again, this is due to the need to keep the peak amplitude below X_{max} for all frequencies. It also implies that a WEC featuring the novel excitation system has the advantage for the designer of a small variation in the optimal damping parameter when compared to the traditional system.

3.6 Future Work on the Numerical Model

The initial goal of the numerical model of the wave energy converter was to examine the potential mass modulation scheme and explore its applicability to the WEC. We believe that the developed model, despite its simplicity, has shown that the proposed mass modulation method can indeed improve the energy harvesting capabilities of a buoy-type WEC. These findings led us to the construction of an experimentally tested scale prototype, discussed in the next chapter.

In the meantime, the model can be further refined, which will lead to optimization of

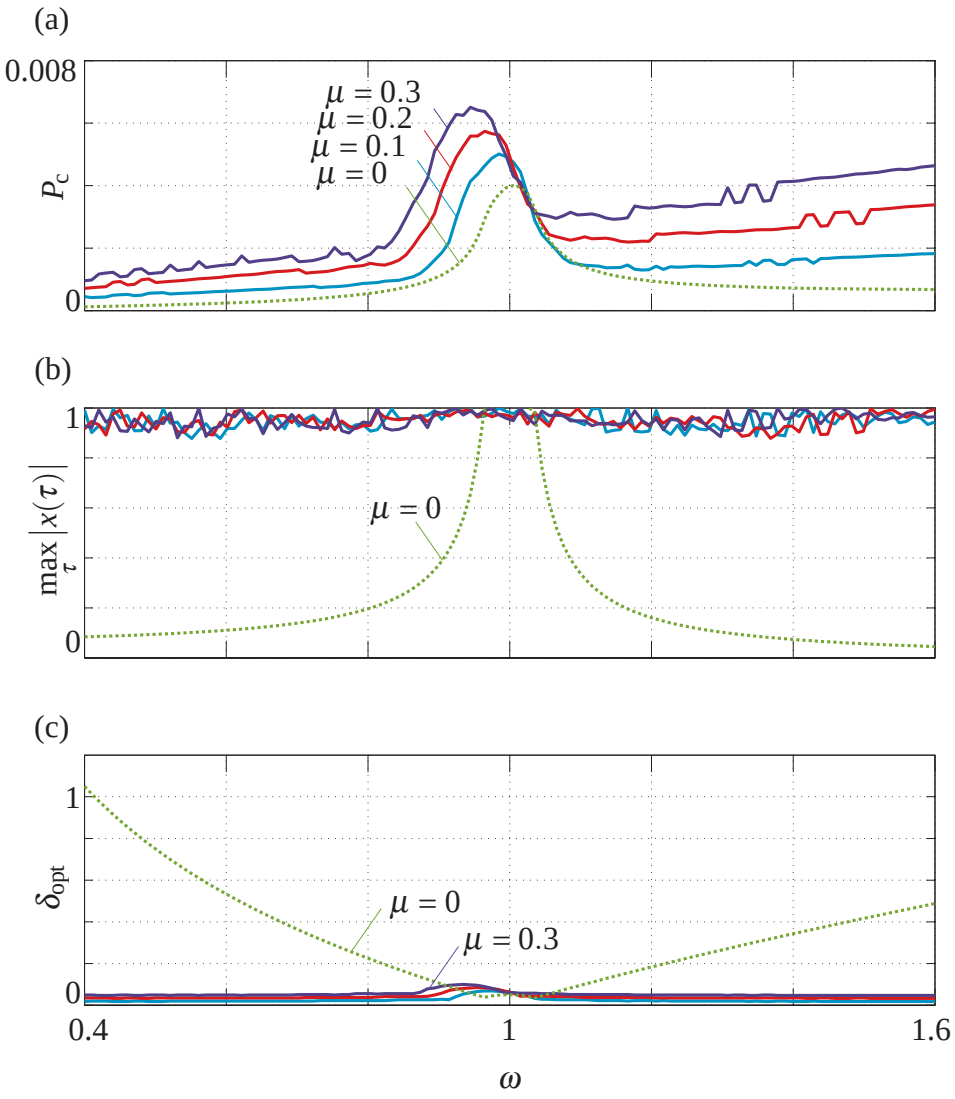

Fig. 26 (a) Average power per cycle, (b) maximum response amplitude, and (c) optimal damping coefficients δ_{opt} as functions of driving frequency ω for μ values of 0, 0.1, 0.2 and 0.3 as indicated on the figure. The case where mass is not modulated is shown with a dashed line. Simulations were performed using $f = 0.1$ and $X_{max} = 1$

the water intake mechanism design. A number of things would need to be improved. Our current method of modeling the damping effects would need to be changed. Two separate damping factors will have to be introduced - one that accounts for hydrodynamic damping (which, being geometry dependent, will need to change between the two switched states), and another that models the power takeoff system. The latter being controllable, would have direct effects on the stability of the system.

The model would also benefit from the introduction of additional degrees of freedom that deal with pitch and roll behaviors of an ocean going WEC, and their possible coupling with the primary heaving mode can be studied. Mooring considerations would need to be taken into account. Finally, in an attempt to closer approximate actual ocean waves, stochastic excitation should be incorporated.

Chapter 4

Experimental Testing

To show the potential of the novel excitation scheme, outlined in Chapter 2 and numerically demonstrated in Chapter 3, a scale prototype of a wave energy converter with a water intake mechanism was constructed and tested in a tow tank facility. This chapter presents the discussion of the performed experimental work and the analysis of the collected data.

4.1 The Experimental Facilities

To understand and improve the performance of the WEC with the water intake mechanism, the prototype had to be tested in a controlled environment that could be readily replicated. To this end, the tow tank facility at the UC Berkeley's Richmond Field Station[1] was employed. The facility houses a 67 meter long, 2.4 meter wide and 1.5 meter deep (at the deepest point) water basin. One end of the basin contains a wavemaker, while the opposite end uses a sloping beach to terminate the waves and reduce wave reflections.

The wavemaker consists of a vertical metal plate, hinged at the bottom, that is hydraulically actuated to push the water along the length of the tank. The plate's harmonic forward and backward motion generates the waves. The motion amplitude and frequency are electronically controlled, thus giving the users the ability to set the wave frequency and amplitude as well. A movable platform, set atop the water basin is used to position and moor the experimental prototype in the water. The schematic and photos of the tow tank facility are is shown in Fig. 27.

4.2 The Simplified Mass Modulation Scheme

While the original mass modulation scheme, proposed in Section 2.2, offers the greatest potential, there are certain challenges when implementing it physically. For example, if the motion frequency of the device is high enough, we found that there will be a significant amount of interference effects between the upper and the lower sets of flaps. Additionally,

[1] http://rfs.berkeley.edu

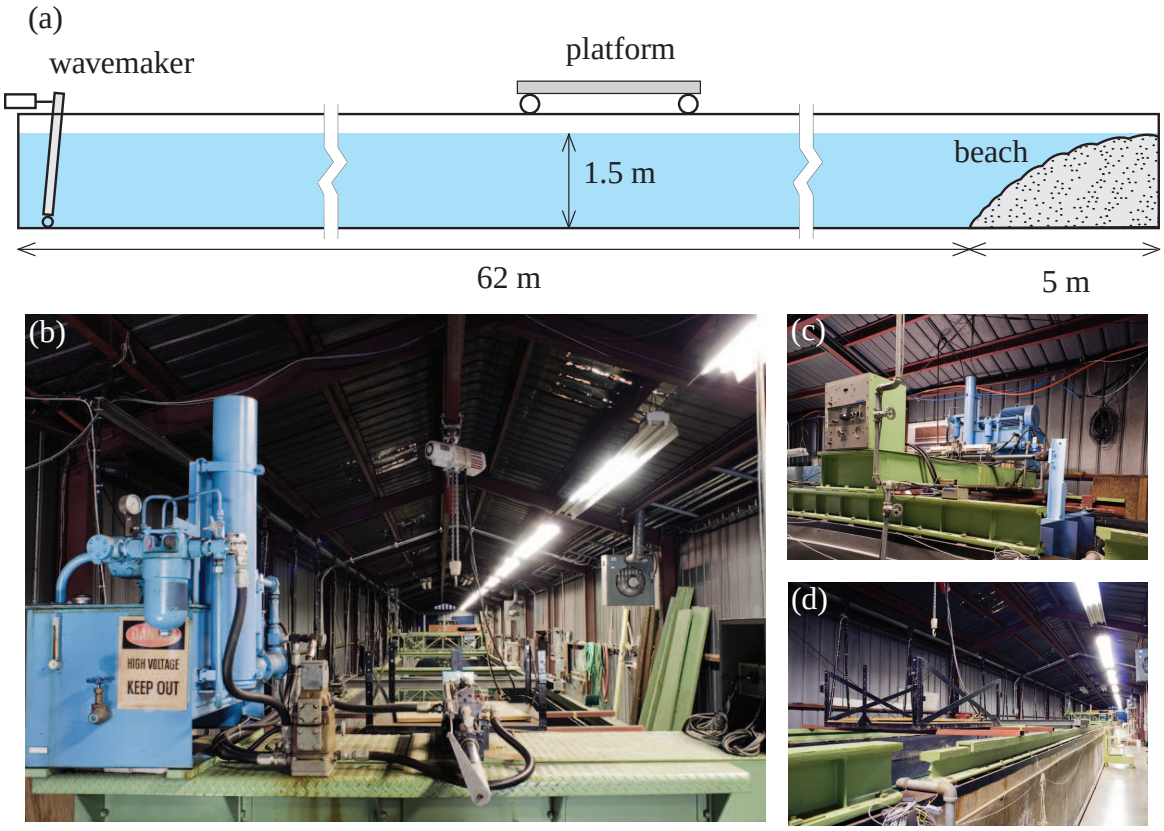

Fig. 27 (a) Schematic of the RFS tow tank facility; (b-d) photos of the facility with the wavemaker mechanism shown in (c)

synchronizing the motion of the flaps and locking them in position at higher frequencies turned out to be a challenging design problem.

To simplify experimental testing, a modified mass modulation scheme has been used. Instead of having an upper and a lower set of butterfly flaps, the water intake system contains only the upper pair of flaps. The upper flaps trap water in the first quarter period of the incidental wave's motion, and allow the water to flow through the submerged cylinder at all other times. The modified scheme is illustrated in Fig. 28. Because there is only one set of flaps, this simplifies the flap locking mechanism as well. It also eliminates the need for sliding plates (item 6 in Fig. 7) and relies on a spring-loaded latch (and the natural hydrodynamic delay) to keep the upper flaps open in the fourth quarter-period (from point *d* to point *a* of the next cycle). The latch also serves to prevent the flaps from prematurely opening as the system slows down before point *b*. In all other aspects, the system is identical in operation to the originally proposed design.

Following the approach in Section 3.2, the stability curve for the unforced system with simplified mass modulation is shown in Fig. 29. The stability curve for the original mass modulation is plotted for comparison.

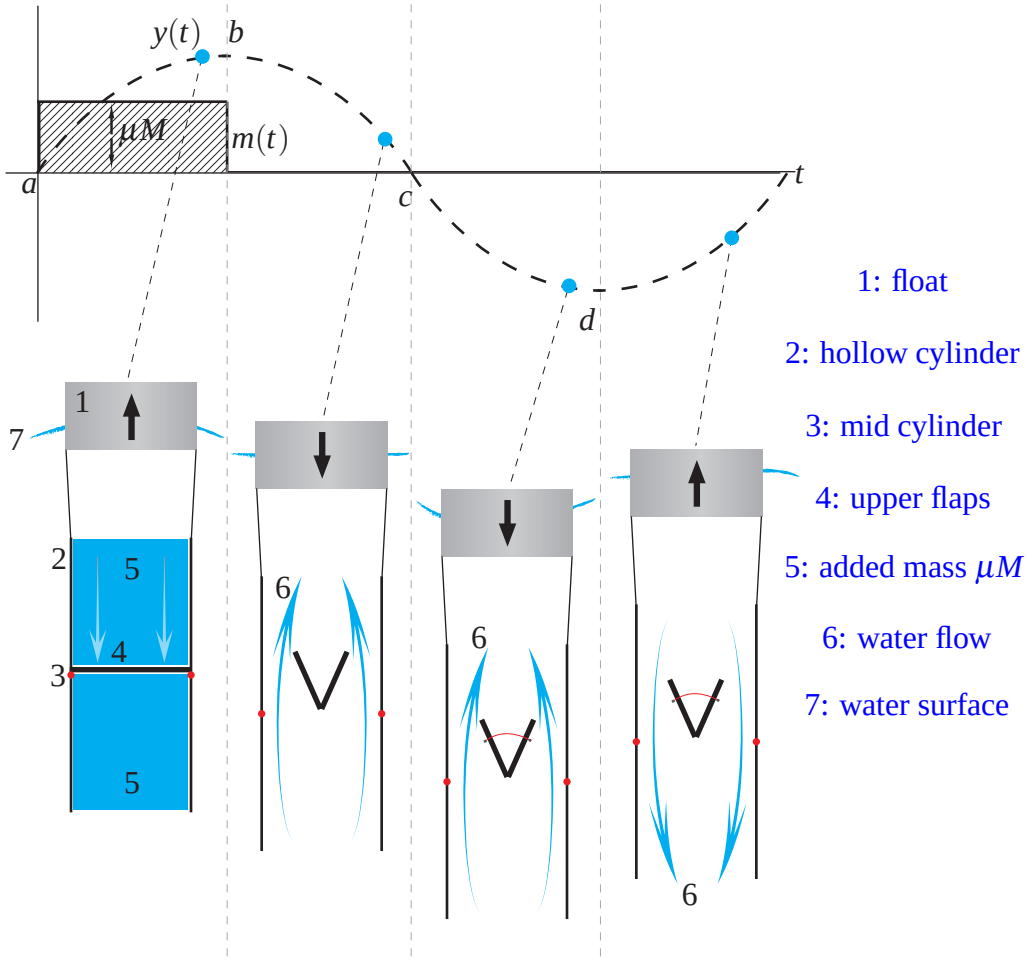

Fig. 28 Illustration of the simplified mass modulation scheme with only the upper flaps present

Numerical simulations of this simplified modulation scheme show that while not as effective as the originally proposed scheme, it is still able to generate an increase in oscillation amplitude and improve the harnessed power over a non-mass modulated WEC. Considering the inherent practical limits on modulation amplitude present in real systems, the performance of this scheme is quite satisfactory. A pair of sample power plots from the simple model are shown in Fig. 30, and Table 3 compares the power output of the simplified scheme to that of the original from Chapter 3.

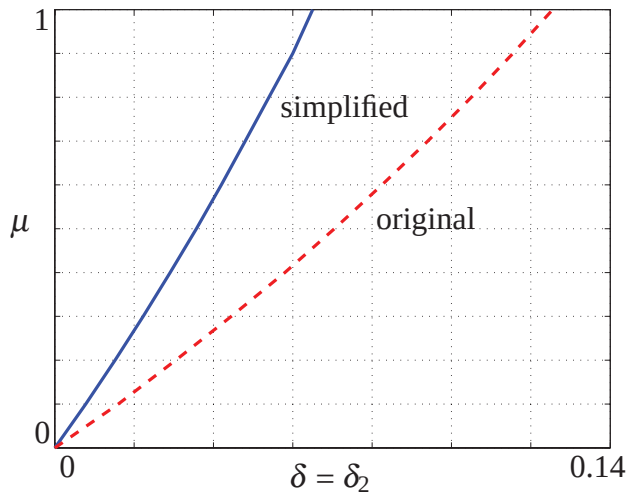

Fig. 29 Stability curves for the unforced system with the simplified mass modulation scheme (solid line) and the original mass modulation scheme (dashed line). The system is stable in the regions to the right of each respective curve

Table 3 Maximum power per cycle $P_{c_{max}}$ for various values of damping factor $\delta = \frac{C}{2\sqrt{KM}}$ and mass modulation parameter μ for the original (F) and simplified (S) mass modulation schemes, and the associated forcing frequency ω at which maximum power occurs. All presented combinations of δ and μ result in a stable system, as discussed in Chapter 3

$P_{c_{max}}$, F / (S)	$\delta = 0.07$	$\delta = 0.12$
$\mu = 0$	0.27 / (0.27)	0.16 / (0.16)
ω @ $P_{c_{max}}$	1.001 / (1.001)	1.001 / (1.001)
$\mu = 0.2$	0.78 / (0.42)	-
ω @ $P_{c_{max}}$	0.956 / (0.980)	-
$\mu = 0.45$	16.6 / (0.79)	-
ω @ $P_{c_{max}}$	0.906 / (0.952)	-
$\mu = 0.5$	-	0.81 / (0.2)
ω @ $P_{c_{max}}$	-	0.900 / (0.910)
$\mu = 0.9$	-	31.3 / (0.47)
ω @ $P_{c_{max}}$	-	0.838 / (0.918)

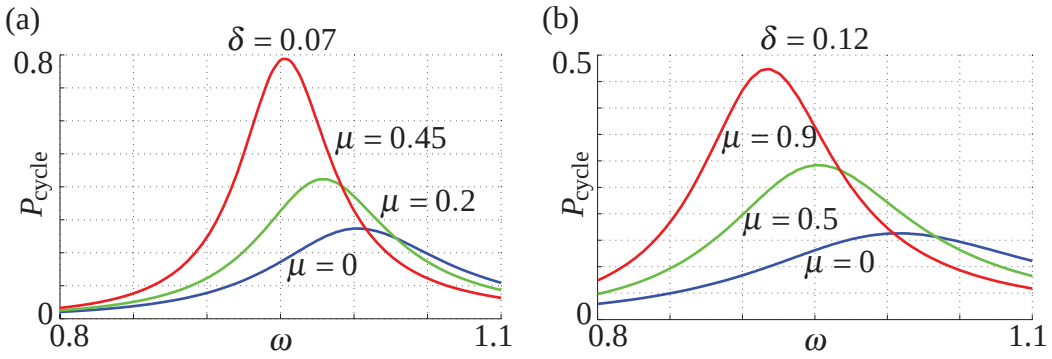

Fig. 30 Average power per cycle P_{cycle} for the simplified mass modulation scheme as a function of driving frequency ω for selected values of damping factor $\delta = \frac{C}{2\sqrt{KM}}$ as indicated on the figure. Here ω is the non-dimensional frequency $\omega = \frac{\omega_f}{\omega_n}$. For these simulations $\omega_n = 1$. Maximum power per cycle for each case is shown in Table 3

4.3 The Scale Prototype

4.3.1 Design and Construction

The scale prototype is comprised of three main parts: 1) the outer float and guides, 2) the inner float, concentric with the outer float and 3) the water intake mechanism, which is rigidly attached to the inner float. While no power takeoff system has yet been implemented, the relative motion of the two floats is used to quantify system performance.

The outer float (see Fig. 32) consists of a 127 mm (5″) high, 381 mm (15″) inner diameter and 660 mm (26″) outer diameter rubber tire tube, filled with air and attached from below to a round 6 mm (0.25”) thick polycarbonate platform. The inflated tube provides the necessary buoyancy, while its relatively large size helps stabilize the motion of the WEC and limit it to mostly vertical excursions. Attached to the polycarbonate platform is a hollow acrylic cylinder that is 762 mm (30″) long, has an outer diameter of 254 mm(10″) and 6 mm (0.25″) wall thickness with six 279 mm (11″) by 191 mm (7.5″) cutouts in its walls. The cutouts ensure that the inner float, which slides vertically inside this cylinder, is exposed to incident waves and is not sheltered from them by the outer float. On the inside of this cylinder are three vertical polycarbonate U-channels that act as motion guides for the inner float and water intake mechanism. The guides were deemed necessary because earlier experiments with an unguided inner float revealed excessive roll and pitch of the inner float relative to the outer float, in effect preventing the inner float from moving vertically with sufficient velocity.

The inner float consists of a hollow acrylic cylinder, 356 mm (14″) long, 203 mm (8″) OD and 6 mm (0.25″) wall thickness. The cylinder is hermetically capped on both ends with a removable top cap. To control the amount of buoyancy the inner float has, it can be partially filled with water. During experimental testing it was filled with water to 229 mm

Table 4 System masses

Outer float	13.4 kg
Inner float, dry	2.7 kg
Inner float with water	9.2 kg
Water intake with connecting links and flaps	3.3 kg
Entrapped water	11.3 kg

(9″), as measured from its bottom (see Fig. 33). On the outside of the cylinder there are three vertical aluminum links that connect the water intake mechanism to the inner float. The links are sufficiently long to position the top of the water intake mechanism 362 mm (14.25″) below the bottom of the inner float. These links use two acetal/delrin sliders each that fit inside the vertical guides of the outer float.

The water intake mechanism also uses an 203 mm (8″) OD hollow open-ended acrylic cylinder that is 406 mm (16″) in length. Around the vertical center of the cylinder are four steel gear rods: two for the upper flaps and two for the lower flaps (see Fig. 31). The upper gears mesh with each other, as do the lower. The meshing gears are required to synchronize the motion of the flaps. In addition, there is a provision to install an intermediate gear that allows the upper gears to mesh with the lower ones when both sets of flaps are installed. Each gear rod runs across the cylinder's cross section, is supported by delrin bearings on each end, and contains a machined slot into which the acrylic semi-circular flap can be inserted and secured via a set-screw. The flaps are made out of 3.18 mm (0.125″) thick acrylic stock. They are 191 mm (7.5″) long and 90 mm (3.5″) wide. As mentioned above, only the upper pair of flaps were installed for the experiments described below. The complete assembled device with both sets of flaps is shown in Fig. 32, and a dimensioned schematic for the inner float is shown in Fig. 33. The weights for the system components are given in Table 4.

4.3.2 The Latching Mechanism

To prevent the upper flaps from closing too soon after the bottom of the cycle has been reached at point *d* in Fig. 28, and from opening prematurely before the top of the cycle is reached at point *b*, a spring loaded latching mechanism has been implemented, shown in Fig. 34. The mechanism consists of: 1) steel cam, attached to one of the upper flaps' gear shafts, 2) aluminum horizontal beam with a brass roller on one end, pivoted on a delrin bearing, 3) aluminum sliding follower with a brass roller on the bottom, 4) compression spring, 5) steel threaded shaft with spring preload adjuster, 6) extension spring and 7) mounting plate.

The mechanism operates as follows. While the upper flaps are open (between points *b* and *d* in Fig. 28), the cam (1) stays above the beam's roller. After point *d* when the

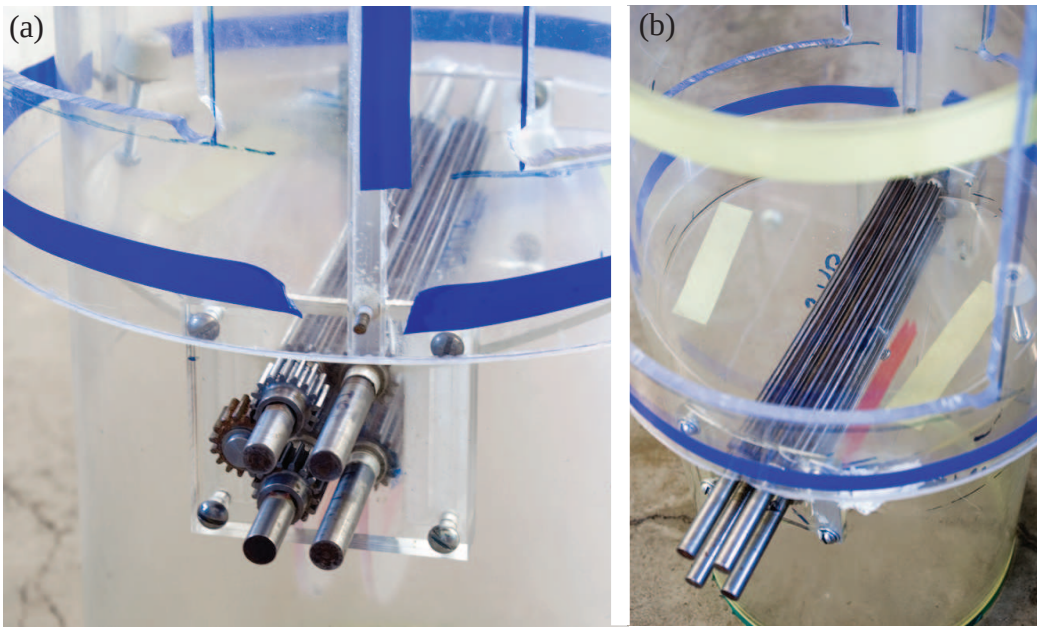

Fig. 31 Flaps in the water intake system. (a) Intermediate gear, connecting the upper and lower flap gears together; (b) upper flaps (marked by yellow tape) are closed, while the lower flaps (red tape) are open. The positioning of the flaps relative to one another is adjustable

water intake is moving up in the fourth quarter-period, the increased water pressure from above is attempting to push the flaps downward into the closed position. The magnitude of this pressure increases with the WEC's upward velocity, which reaches its peak at point *a*. The spring is used to provide enough resistance to delay the beam (2) swinging down until point *a* is reached and the flaps close (Fig. 34(b)). Because the preload on the spring is adjustable, so is its resistance. This allows fine-tuning the device's operation at each excitation frequency.

Once the resistance of the spring has been overcome at point *a*, the cam pushes the beam down (Fig. 34(c)), rotates past it, and stops to rest below it when the flaps are closed (Fig. 34(d)). When the system slows down near the top of the cycle, the inertia of the flaps attempts to swing them up (i.e., into the open position). This rotates the cam upwards, which pushes the beam up. The extension spring (6) is installed to prevent this from happening until point *b* is reached. A soft spring has been selected, so when the WEC reverses its direction of motion, the extension spring's resistance is overcome and the upper flaps are allowed to open.

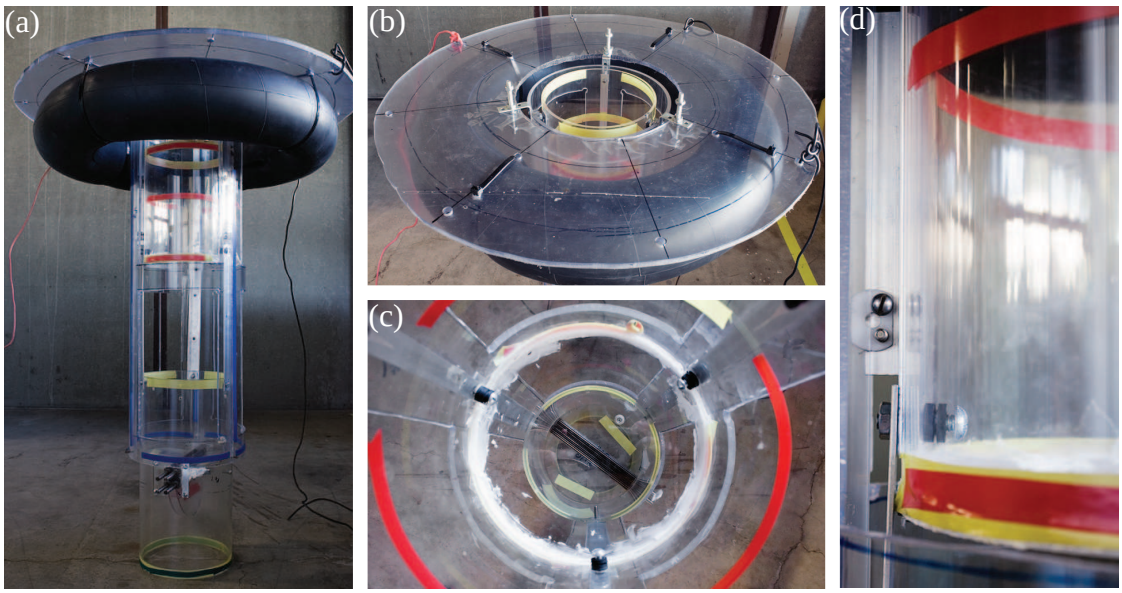

Fig. 32 Images of the scale prototype WEC. (a) Outer float, inner float and the water intake system; (b) outer float with the inner float visible (marked by yellow tape); (c) looking down the inner float, the flaps and their associated gears are visible at the bottom; (d) detail of the guides used to restrict the roll and pitch motions of the inner float

4.3.3 The Data Acquisition System

While no power takeoff system (PTO) has yet been implemented, the performance of the system is currently quantified by calculating the root mean square (RMS) of the difference in vertical velocities between the inner and outer floats. Recall from equation 3.23 in Chapter 3 that the harnessed power is the damping coefficient of the PTO times the integral of the velocity squared. To determine the vertical velocities of the two floats, 3-axis Analog Devices ADXL335 accelerometers are rigidly mounted on each float, as shown in Fig. 35. The accelerometers are outputting data at 100Hz.

The signals from the accelerometers are sent to the Arduino microprocessor board (ground-based), which processes the acceleration readings in real time and sends the data to a personal computer. The initial data processing algorithm smoothes the voltage readings from the accelerometers and converts the readings into acceleration values on a g-scale (where 1g is the vertical acceleration of gravity).

After the acceleration data has been acquired, it is imported into MATLAB. The data are then resampled (to fix any potential omitted time steps in the original data), reformatted, and post-processed by smoothing and double integration of the accelerations to obtain velocities and positions. The difference in vertical velocities of the outer and inner float is also calculated.

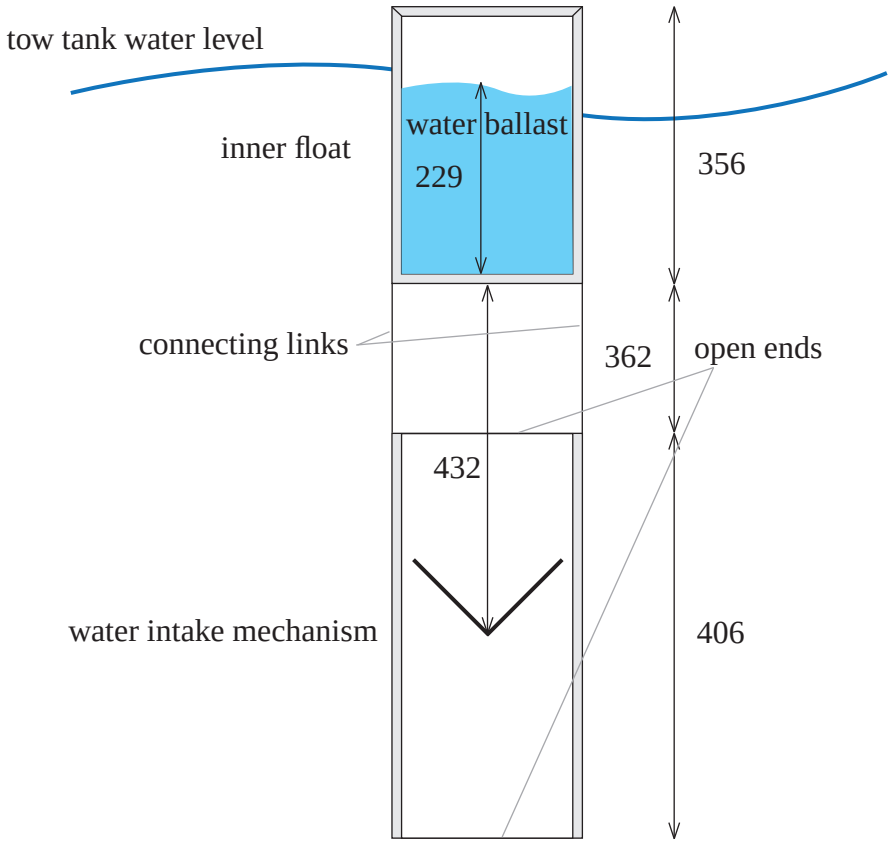

Fig. 33 Schematic of the inner float and water intake system, showing dimensions in mm

4.4 The Testing Procedure

To conduct experimental testing, several excitation frequencies are first selected by observing the response of the WEC to excitation. If the excitation frequency is too low, it fails to produce significant relative motion between the inner and outer floats, both of which follow the waves. Too high a frequency introduces wave reflections, super-harmonics, and results in a highly non-periodic motion of the WEC. The objective during tests was to obtain as harmonic of a wave form as possible. Through trial and error, the useful range of excitation frequencies has been established to be 0.60 Hz $\leq f \leq$ 0.76 Hz. The system is first tested over this range of frequencies with the upper flaps installed and then tested again with the flaps removed. Comparing the two cases reveals whether the proposed mass modulation scheme provides any advantage.

During all tests the outer float was moored to the stationary carriage in the tow-tank using three flexible cables. The cables provided enough slack for the device to move up and down, but limited horizontal motion to prevent the system from drifting and inhibited roll/pitch tendencies. The device was positioned at the center of the tow tank, which pro-

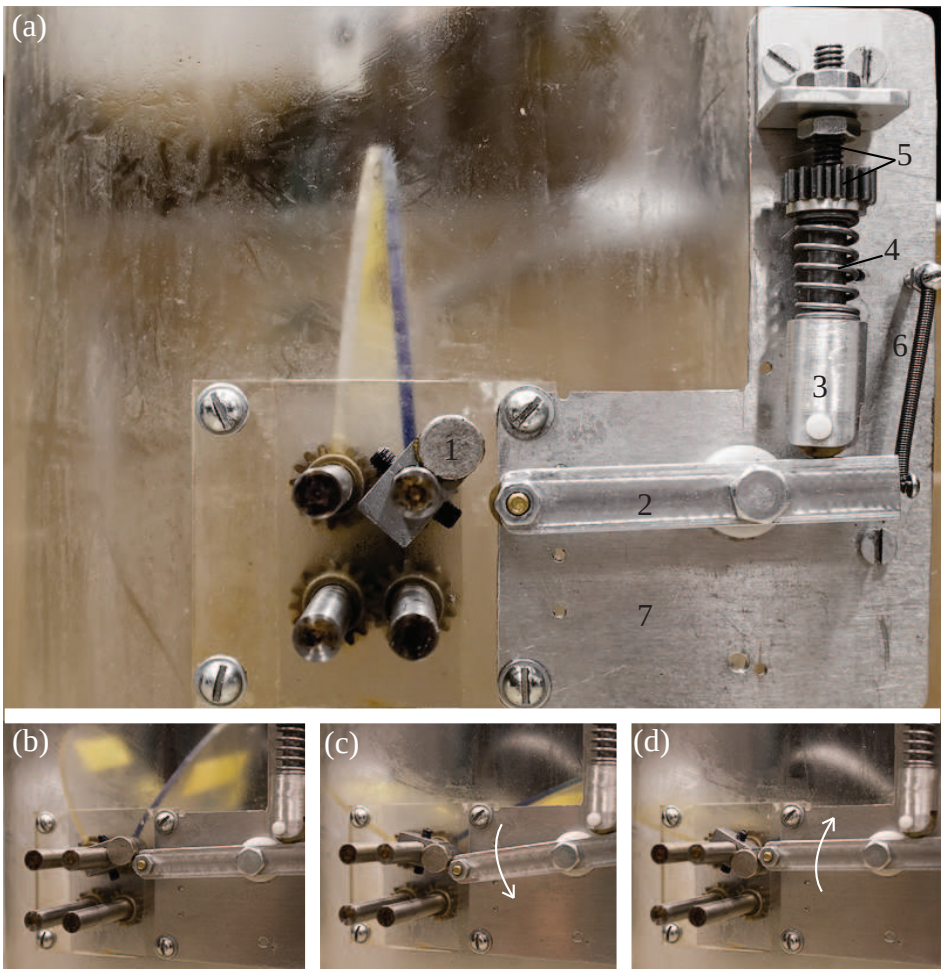

Fig. 34 Photos of the latch mechanism. (a) The mechanism consists of (1) steel cam, attached to one of the upper flaps' gear shafts, (2) aluminum horizontal beam with a brass roller on one end, pivoted on a delrin bearing, (3) aluminum sliding follower with a brass roller on the bottom, (4) compression spring, (5) steel threaded shaft with spring preload adjuster, (6) extension spring and (7) mounting plate. (b) The spring resists the flaps closing. (c) The spring resistance is overcome, pushing the beam down. (d) The flaps move into the closed position

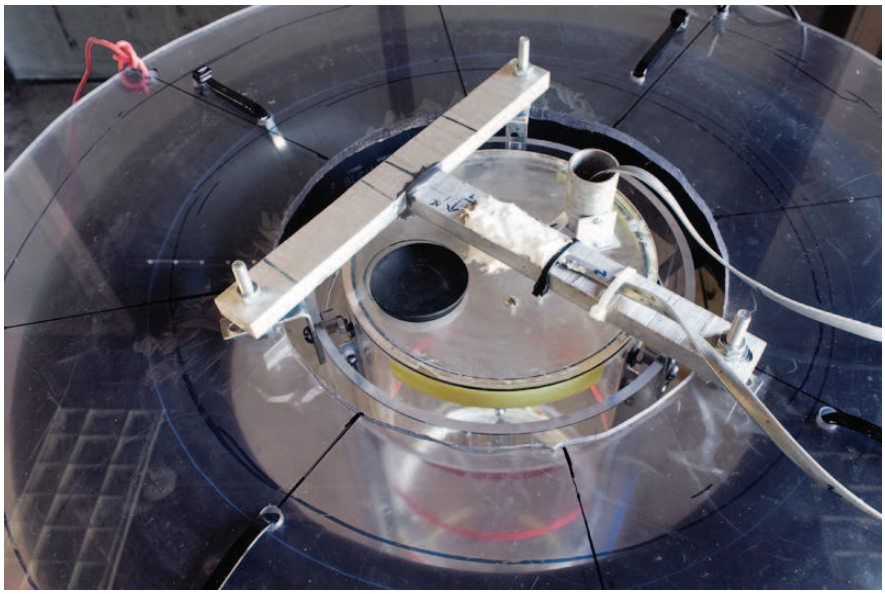

Fig. 35 The 3-axis accelerometers rigidly mounted to the outer (top of the T-beam) and inner (center of the upper cap) floats. The signal cables are connected to the land-based Arduino microcontroller.

vided a 0.4 m clearance between the bottom of the device and the floor of the tow tank. While this does not approximate the setup in the open sea (where the clearance would be much greater), we believe that it provides enough clearance to avoid significant hydrodynamic interference effects from the floor.

With the wavemaker on, the wave amplitude was kept to 10 ± 1 cm for all excitation frequencies. Once a steady state wave climate has been established for a particular frequency, data recording was initiated. After enough data is collected (typically 60-80 seconds worth of samples at 100 Hz sampling rate), the data recording is stopped and the wavemaker is shut off. After all the waves are attenuated and the water surface becomes calm, a new excitation frequency is selected and the cycle begins again.

4.5 Experimental Results and Analysis

Figs. 36-40 show vertical velocity and phase portrait plots for each of the five testing frequencies: 0.60 Hz, 0.64 Hz, 0.68 Hz, 0.72 Hz, and 0.76 Hz. The respective wavelengths, as estimated from the water wave dispersion relation [31] are 4.2 m, 3.8 m, 3.4 m, 3.0 m, and 2.7 m. The data in the figures for each testing frequency are organized as follows. The top row shows the vertical velocity of the inner float v_{i} (blue solid line) and the vertical velocity of the outer float v_{o} (black dashed line). The second row shows vertical velocity difference between the two floats, $\Delta v = v_{\mathrm{i}} - v_{\mathrm{o}}$. The three rows of phase portraits show vertical velocity v_{i} vs. vertical position x_{i} for the inner float, vertical velocity v_{o} vs. position

Table 5 Comparison of the experimental data for the five testing frequencies. Note that the resonant frequency for the prototype is estimated to be between 0.64 Hz and 0.68 Hz

f, Hz	$\Delta v^{\mathrm{RMS}}{}_{\text{no flaps}}(m/s)$	$\Delta v^{\mathrm{RMS}}{}_{\text{flaps}}(m/s)$	$v_{\mathrm{i}}^{\mathrm{RMS}}{}_{\text{no flaps}}(m/s)$	$v_{\mathrm{i}}^{\mathrm{RMS}}{}_{\text{flaps}}(m/s)$
0.60	0.041	0.038	0.122	0.118
0.64	0.076	0.066	0.133	0.138
0.68	0.075	0.086	0.137	0.138
0.72	0.117	0.118	0.151	0.169
0.76	0.117	0.086	0.141	0.171

x_{o} for the outer float, and relative vertical velocity Δv vs. relative vertical position $\Delta x = x_{\mathrm{i}} - x_{\mathrm{o}}$ between the two floats, respectively. The cases with no flaps are shown on the left, while the cases with upper flaps installed are shown on the right.

To determine system performance, a set of metrics needs to be established. In this case, we use the root mean square (RMS) of the velocity difference $\Delta v^{\mathrm{RMS}} = \sqrt{\overline{\Delta v}}$ and the RMS of the vertical velocity of the inner float $v_{\mathrm{i}}^{\mathrm{RMS}} = \sqrt{\overline{v_{\mathrm{i}}}}$ as the performance metrics for each run. For example, if $v_{\mathrm{i}}^{\mathrm{RMS}}$ and Δv^{RMS} turn out to be greater in the case of the upper flaps installed, compared to the case with no flaps, the mass modulated system is deemed to outperform the base system at that wave frequency because the mass modulation increases the inner float's velocity, and the associated higher velocity differential improves the power harnessing capabilities of the system. If, on the other hand, $v_{\mathrm{i}}^{\mathrm{RMS}}$ is greater for the upper flaps' case, but Δv^{RMS} is smaller, this implies that while the mass modulation leads to an increase in inner float's velocity, the phase separation between the inner and outer floats in the case with flaps is not advantageous. It is observed that the vertical velocities of the two floats are coupled. Table 5 lists the performance metrics for all five testing frequencies.

4.5.1 0.60 Hz

The results for the excitation frequency 0.60 Hz are shown in Fig. 36. Looking at the performance metrics, it is apparent that the base system performs better than the mass modulated one at this frequency. During the experiments it was observed that the WEC prototype did not have a significant response to the excitation either with or without flaps. This is attributed to the fact that the forcing frequency for this case was too far away from the resonant frequency of the device. As a consequence, there was not enough momentum in the prototype's motion to enable the full movement of the flaps. While the flaps were able to fully close, there was not enough fluid momentum to completely open the flaps. Thus, with the mass modulation not working as intended, the flaps created extra drag on the system, resulting in a worse performance than the non-mass modulated case.

Comparing the vertical velocity plots in Fig. 36(a, b), we note that there is not much

separation in the motion of the two floats. Essentially, both the inner and outer floats are following the oncoming waves. Otherwise, the motions of the system with flaps and without are quite similar. The small troughs near the peaks of the velocity curves are attributed to rolling and pitching of the device. From the phase portraits in Fig. 36(e)-(h) it can be seen that the inner float has a slightly larger range of motion with the flaps removed, while the outer float moves further when the flaps are installed.

4.5.2 0.64 Hz

The results for the excitation frequency 0.64 Hz are presented in Fig. 37. We note that the resonant frequency of the prototype is deemed to lie between 0.64 Hz and 0.68 Hz. The performance metrics show that while the inner float velocity is higher with the mass-modulated WEC, the velocity differential is lower when the flaps are installed. However, unlike the case of 0.60 Hz, the prototype exhibited a response to wave excitation. This provided enough momentum to operate the flaps, as evidenced from the velocity plots in Fig. 37(b) and the phase portrait in Fig. 37(f). A distinct drop in the vertical velocity can be seen when the flaps close just past the point of maximum velocity. This effect is more pronounced at the higher excitation frequencies of 0.68 Hz and 0.72 Hz.

4.5.3 0.68 Hz

The results for the excitation frequency 0.68 Hz, which is close to the device's resonant frequency, are shown in Fig. 38. Examining the vertical velocity plots as a function of time and the corresponding performance metrics, we see that $v_{\mathrm{i}}^{\mathrm{RMS}}$ values are quite close to each other for the two cases. At the same time, from the shape of the plots it is apparent that, on average, the peak v_{i} values with the flaps installed (Fig. 38(b)) are actually greater than when the flaps are removed, but the "broader" shape of the v_{i} plot in Fig. 38(a) contributes to phase separation.

We note that Δv^{RMS} with flaps is greater than without flaps, even though the values of $v_{\mathrm{i}}^{\mathrm{RMS}}$ and $v_{\mathrm{o}}^{\mathrm{RMS}}$ with mass modulation are close to each other. Nonetheless, the magnitudes of Δv^{RMS} are lower at 0.68 Hz compared to the higher excitation frequencies, suggesting that the phase separation between the two floats could be improved.

Examining the phase portraits for the inner float in Fig. 38(e, f), we can observe the distinctive kink in the plot on the right when the upper flaps close, as well as greater peak velocity for this case. Fig. 38(g, h) shows the phase portraits for the outer float in the two cases. Apparent is the greater travel for the outer float in the no flaps case, while the peak velocity is greater for the case with flaps installed. Finally, while the phase portraits of the difference in Fig. 38(i, j) may be difficult to judge due to the inconsistent orbits, we can observe greater Δv for the flaps case on several occasions, which explains the Δv^{RMS} value difference between the two cases.

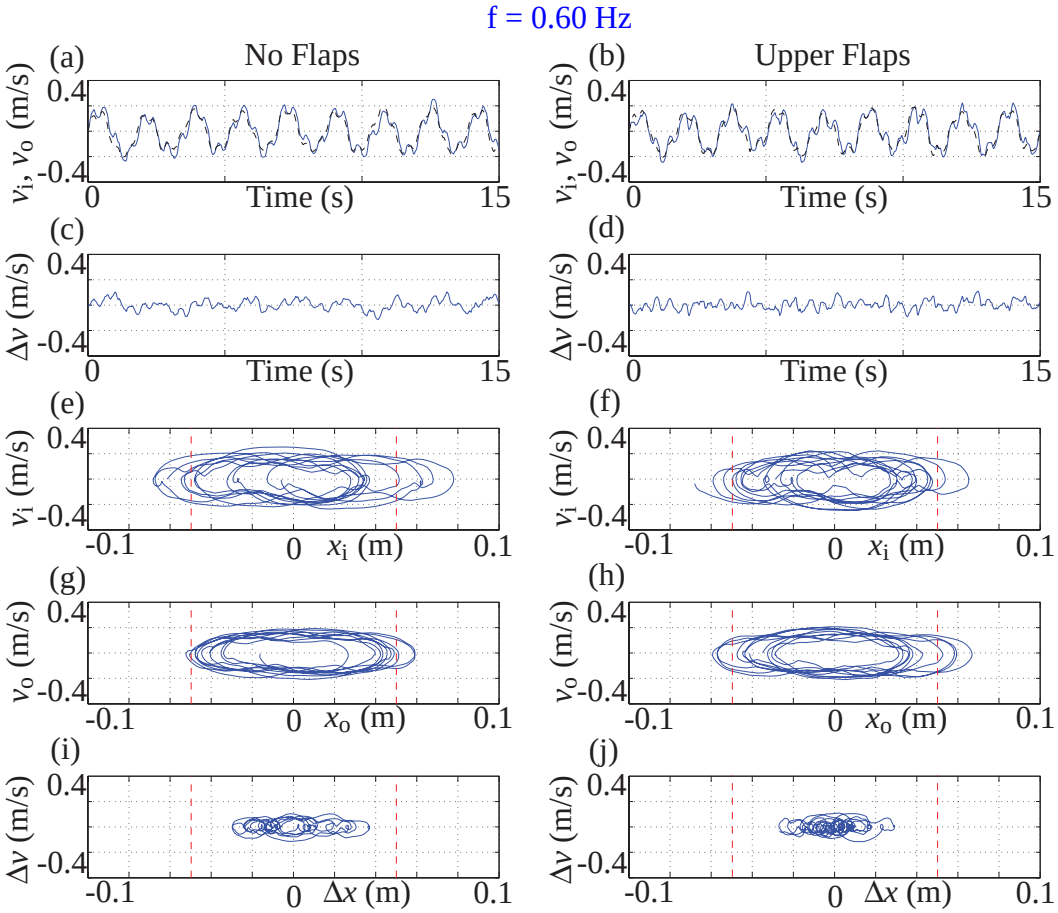

Fig. 36 Experimental data for the wave excitation frequency 0.60 Hz. Left: flaps removed, $\Delta v^{\mathrm{RMS}} = 0.041$ m/s, $v_{\mathrm{i}}^{\mathrm{RMS}} = 0.122$ m/s, $v_{\mathrm{o}}^{\mathrm{RMS}} = 0.115$ m/s. Right: upper flaps installed, $\Delta v^{\mathrm{RMS}} = 0.038$ m/s, $v_{\mathrm{i}}^{\mathrm{RMS}} = 0.118$ m/s, $v_{\mathrm{o}}^{\mathrm{RMS}} = 0.119$ m/s. (a, b) Vertical velocity of inner (solid line) and outer (dashed line) floats as a function of time; (c, d) Vertical velocity difference $\Delta v = v_{\mathrm{i}} - v_{\mathrm{o}}$ between the inner and outer floats; (e, f) inner float position x_{i} vs. inner float velocity v_{i}; (g, h) outer float position x_{o} vs. outer float velocity v_{o}; (i, j) position difference Δx vs. velocity difference Δv between the inner and outer floats. The dashed vertical lines in (e)-(j) mark ± 5cm, corresponding to the 10 cm peak-to-peak wave amplitude

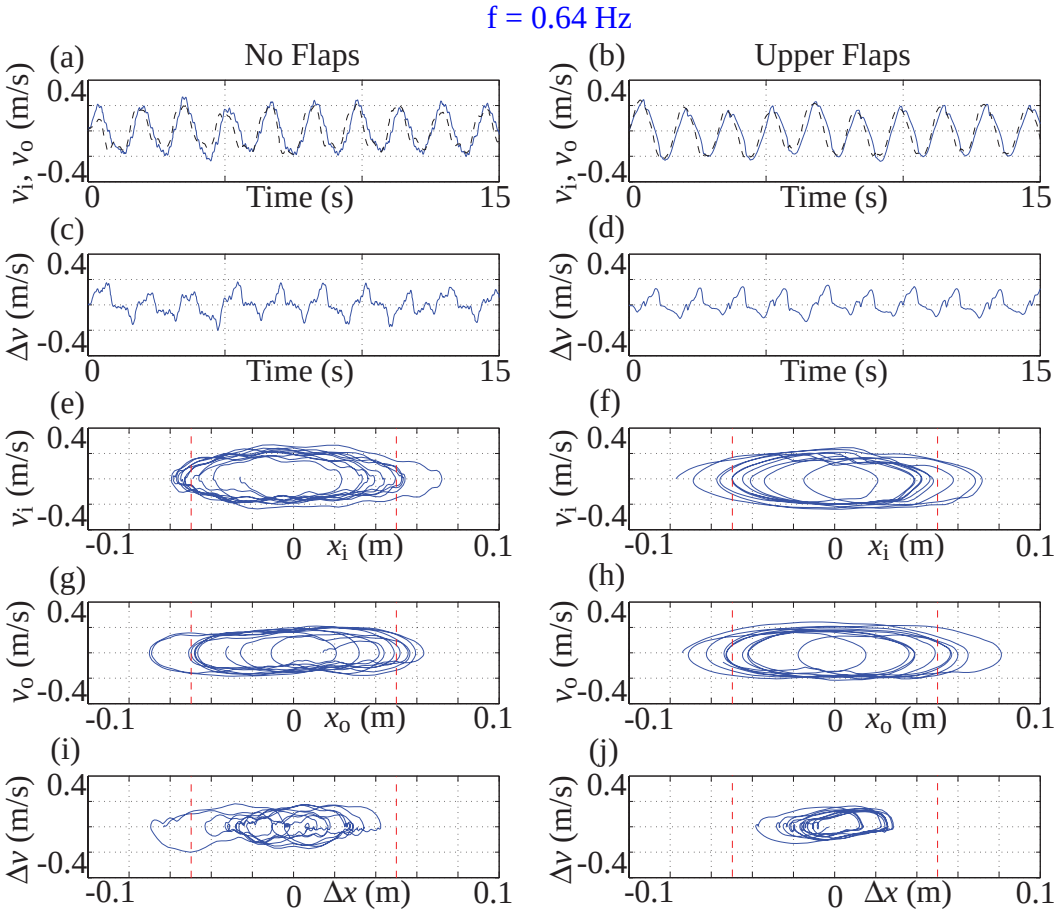

Fig. 37 Experimental data for the wave excitation frequency 0.64 Hz. Left: flaps removed, $\Delta v^{\mathrm{RMS}} = 0.076$ m/s, $v_{\mathrm{i}}^{\mathrm{RMS}} = 0.133$ m/s, $v_{\mathrm{o}}^{\mathrm{RMS}} = 0.120$ m/s. Right: upper flaps installed, $\Delta v^{\mathrm{RMS}} = 0.066$ m/s, $v_{\mathrm{i}}^{\mathrm{RMS}} = 0.138$ m/s, $v_{\mathrm{o}}^{\mathrm{RMS}} = 0.141$ m/s. (a, b) Vertical velocity of inner (solid line) and outer (dashed line) floats as a function of time; (c, d) Vertical velocity difference $\Delta v = v_{\mathrm{i}} - v_{\mathrm{o}}$ between the inner and outer floats; (e, f) inner float position x_{i} vs. inner float velocity v_{i}; (g, h) outer float position x_{o} vs. outer float velocity v_{o}; (i, j) position difference Δx vs. velocity difference Δv between the inner and outer floats. The dashed vertical lines in (e)-(j) mark ± 5cm, corresponding to the 10 cm peak-to-peak wave amplitude

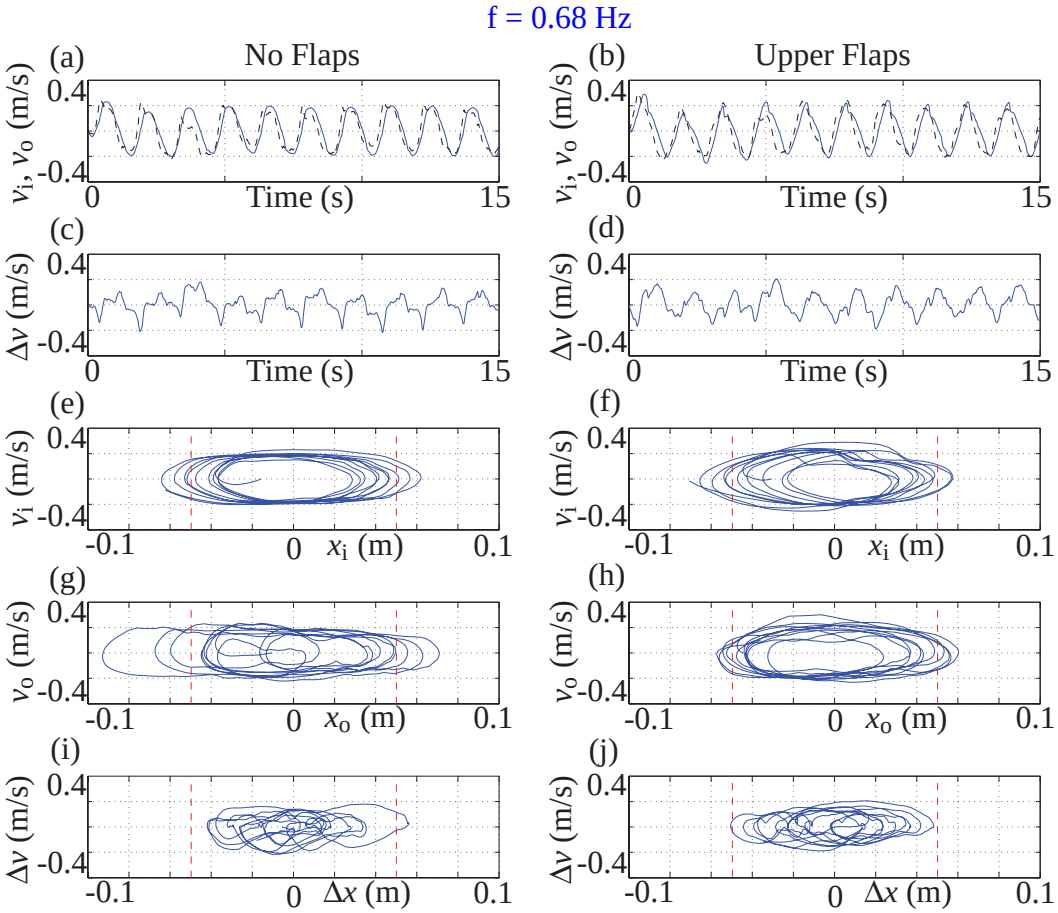

Fig. 38 Experimental data for the wave excitation frequency 0.68 Hz. Left: flaps removed, $\Delta v^{\mathrm{RMS}} = 0.075$ m/s, $v_{\mathrm{i}}^{\mathrm{RMS}} = 0.137$ m/s, $v_{\mathrm{o}}^{\mathrm{RMS}} = 0.132$ m/s. Right: upper flaps installed, $\Delta v^{\mathrm{RMS}} = 0.086$ m/s, $v_{\mathrm{i}}^{\mathrm{RMS}} = 0.138$ m/s, $v_{\mathrm{o}}^{\mathrm{RMS}} = 0.142$ m/s. (a, b) Vertical velocity of inner (solid line) and outer (dashed line) floats as a function of time; (c, d) Vertical velocity difference $\Delta v = v_{\mathrm{i}} - v_{\mathrm{o}}$ between the inner and outer floats; (e, f) inner float position x_{i} vs. inner float velocity v_{i}; (g, h) outer float position x_{o} vs. outer float velocity v_{o}; (i, j) position difference Δx vs. velocity difference Δv between the inner and outer floats. The dashed vertical lines in (e)-(j) mark ± 5cm, corresponding to the 10 cm peak-to-peak wave amplitude

4.5.4 0.72 Hz

The results for the excitation frequency 0.72 Hz are shown in Fig. 39. The velocity of the inner float, v_i, with the flaps installed is now significantly higher than in the case of no flaps. The same comment applies to the velocity of the outer float, v_o, suggesting the motions of the two floats are coupled. However, the velocity difference between the floats, Δv, is almost equal with flaps and without, even though the magnitude of this quantity is considerably higher than in the 0.68 Hz case.

The orbits for the phase portraits in Fig. 39(e)-(j) are now more consistent with each other, compared to the 0.68 Hz case. Fig. 39(f) again has the distinctive kink, corresponding to the flaps closing.

4.5.5 0.76 Hz

The results for the excitation frequency 0.76 Hz are shown in Fig. 40. v_i^{RMS} for the inner float with flaps is again higher than without flaps, but Δv for the case with flaps is considerably lower, again due to the fact that the velocity magnitudes of the inner and outer floats are so close to each other in the case of installed flaps. Additionally, as seen in Fig. 40(f), the kink in the orbits for the inner float is less pronounced than at other frequencies, indicating that the motion of the flaps is less precise now. Note in Fig. 40(h) that the orbits for the outer float with the flaps installed appear somewhat tapered. This may suggest an increase in damping, compared to the no flaps case (due to the coupled nature of the motion of the two floats). Finally, all orbits are again appearing aperiodic, which may indicate that the exciting waveforms are no longer clean, resulting in increased pitching and rolling of the prototype.

4.6 Results Summary

Several conclusions can be drawn from the experimental results presented above. Aside from the low frequency case of 0.60 Hz, the inner float's vertical velocity has been higher with the mass modulated system for the tests presented above. Also of note is that potential power extraction, as measured by Δv^{RMS}, increases near the system's resonant frequency. This leads us to believe that the mass modulation is capable of improving the performance of the WEC. However, with a design that relies on relative motion between two floats to harness energy, it is also important to achieve a good phase separation between them, thereby increasing Δv. The current prototype exhibits fairly close coupling between the two floats, which appears to be frequency dependent. It is important to better understand this behavior and build in sufficient flexibility to control the float phase separation. This will be attempted in our future work.

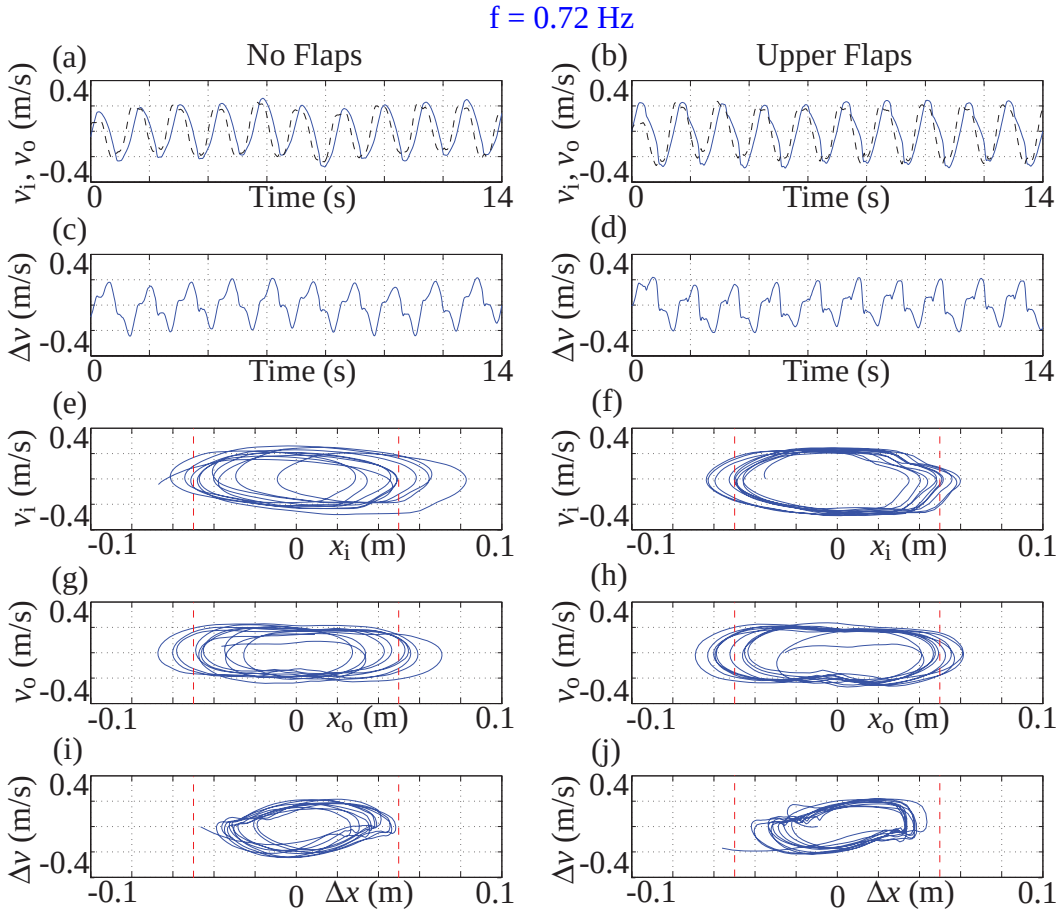

Fig. 39 Experimental data for the wave excitation frequency 0.72 Hz. Left: flaps removed, $\Delta v^{\mathrm{RMS}} = 0.117$ m/s, $v_{\mathrm{i}}^{\mathrm{RMS}} = 0.151$ m/s, $v_{\mathrm{o}}^{\mathrm{RMS}} = 0.149$ m/s. Right: upper flaps installed, $\Delta v^{\mathrm{RMS}} = 0.118$ m/s, $v_{\mathrm{i}}^{\mathrm{RMS}} = 0.169$ m/s, $v_{\mathrm{o}}^{\mathrm{RMS}} = 0.165$ m/s. (a, b) Vertical velocity of inner (solid line) and outer (dashed line) floats as a function of time; (c, d) Vertical velocity difference $\Delta v = v_{\mathrm{i}} - v_{\mathrm{o}}$ between the inner and outer floats; (e, f) inner float position x_{i} vs. inner float velocity v_{i}; (g, h) outer float position x_{o} vs. outer float velocity v_{o}; (i, j) position difference Δx vs. velocity difference Δv between the inner and outer floats. The dashed vertical lines in (e)-(j) mark ± 5cm, corresponding to the 10 cm peak-to-peak wave amplitude

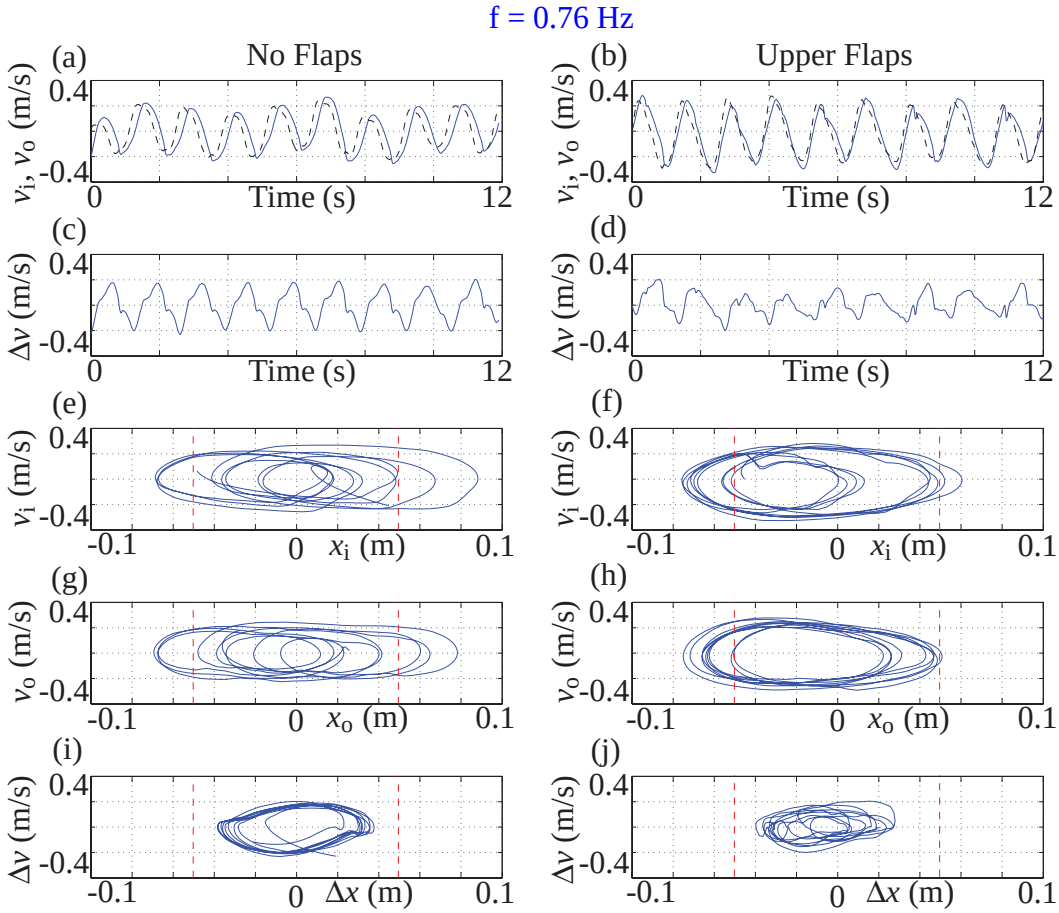

Fig. 40 Experimental data for the wave excitation frequency 0.76 Hz. Left: flaps removed, $\Delta v^{\mathrm{RMS}} = 0.117$ m/s, $v_{\mathrm{i}}^{\mathrm{RMS}} = 0.141$ m/s, $v_{\mathrm{o}}^{\mathrm{RMS}} = 0.136$ m/s. Right: upper flaps installed, $\Delta v^{\mathrm{RMS}} = 0.086$ m/s, $v_{\mathrm{i}}^{\mathrm{RMS}} = 0.171$ m/s, $v_{\mathrm{o}}^{\mathrm{RMS}} = 0.172$ m/s. (a, b) Vertical velocity of inner (solid line) and outer (dashed line) floats as a function of time; (c, d) Vertical velocity difference $\Delta v = v_{\mathrm{i}} - v_{\mathrm{o}}$ between the inner and outer floats; (e, f) inner float position x_{i} vs. inner float velocity v_{i}; (g, h) outer float position x_{o} vs. outer float velocity v_{o}; (i, j) position difference Δx vs. velocity difference Δv between the inner and outer floats. The dashed vertical lines in (e)-(j) mark ± 5cm, corresponding to the 10 cm peak-to-peak wave amplitude

Chapter 5

Conclusions and Future Work

As mentioned, the long term goal of this research undertaking is to develop a reliable mass modulation mechanism for wave energy converters to improve their power harnessing capabilities. The primary intent of the work presented in this dissertation, however, was to demonstrate the viability of the mass modulation scheme, prove the concept of the water intake mechanism, and lay the groundwork for future developments. Based on the experimental data presented in Chapter 4, we believe the intent has been successfully satisfied. There are, however, a number of issues that would need to be addressed with future undertakings, as well as several directions that the work in this dissertation can be branched out in. They are outlined below.

5.1 Numerical Model

From the onset, our numerical model for the wave energy converter with mass modulation has been purposefully kept simple. This allowed us to isolate the effects of mass modulation and clearly see if this scheme holds potential. Having gained the fundamental understanding, the model should now be further developed to closer approximate the behavior of the experimental prototype.

The key aspect of the numerical model that needs improvement is the damping. Instead of using a common damping factor for the hydrodynamic effects and the power takeoff mechanism, the two need to be separated. Further, since hydrodynamic damping is shape dependent, the appropriate coefficients would need to change between the two switched states. Additionally, hydrodynamic added mass (distinct from the mass added by trapping water) and more accurate modeling of stiffness (effectively, the buoyancy force) should be attempted. Boundary element modeling can be used to calculate the damping and hydrodynamic added mass coefficients.

Due to the nature of wave forcing, the actual prototype goes through non-negligible rolling and pitching motions that are coupled with heaving. To gain a better understanding of the mode coupling and potential ways of mode isolation, these motions should be included in the revised model, introducing additional degrees of freedom. This would be

far from simple, as the additional modes require their own set of coefficients that may be challenging to compute due to their dependence on orientation.

Finally, the model would significantly benefit from the introduction of stochastic excitation to approximate ocean waves more accurately. An understanding of the effect that multiple simultaneous forcing frequencies have on the mass modulated wave energy converter will be a big aid in prototype development.

The new aspects of the model will naturally make it more complicated. Care should be taken to ensure that the added complexity does not detract from the understanding of the physical phenomena being modeled. With so many additional variables, it can be difficult to clearly distinguish the effects of each parameter on the behavior of the model. Nonetheless, the addition of new parameters will produce some very interesting results. The study of the system stability could easily turn out to be a separate topic.

5.2 Experimental Prototype

Alongside the development of the numerical model, prototype improvements should be ongoing. Much like the numerical model, the current version of the prototype has been designed with simplicity of construction in mind. As such, there is much room for improving its performance.

The most important component that needs to be introduced is the power takeoff (PTO) mechanism. The addition of the PTO will provide a clear indication whether the water intake mechanism (with flaps installed) leads to improved power absorption, which is the ultimate goal. The PTO could be a purchased unit or could be constructed from available parts and materials. Wavebob (as described in Chapters 1 and 2) uses a hydraulic PTO mechanism. On the current prototype scale, however, we believe a hydraulic PTO would be too complicated. Instead, the PTO could use a permanent magnet linear generator, or a simple linked mechanism to drive a DC motor in reverse. The disadvantage of these systems over a hydraulic setup is the inability to adjust the damping load. However, the latter is not an immediate goal and can be sidestepped for now.

The existing parts of the prototype should also be improved. The latching mechanism should be redesigned to both reduce the number of moving parts, as well as provide more reliable operation. An introduction of an electronic controller (either for spring preload adjustment or to control the entire latching mechanism) is a distinct possibility.

The existing guide mechanism for the inner float consists of acetal sliders in polycarbonate U-channels. Due to the design constraints this was a simple and accessible solution at the time of construction. However, the performance of the guides can be significantly improved. One approach is to use linear bearings that slide on rods attached to the outer float. By reducing friction and significantly decreasing the side loads, this would considerably improve the motion of the inner float relative to the outer one and potentially decouple their motion. If the outer guide tube with cutouts is eliminated as part of the redesign, the inner float will also be able to exhibit an improved response to the incoming waves. When the new design is considered, an increase in the range of vertical motion for the inner float

should also be implemented.

The improvements listed above can be carried out in conjunction with the upper-flaps-only setup. However, since the original mass modulation scheme consisted of two pairs of flaps, the lower flaps should be re-introduced in the prototype at some point. Making them work in tandem with the upper flaps is a far from trivial task, so a better understanding of hydrodynamics at work will be required. It may be necessary to increase the mass of the prototype to allow it to successfully operate at lower wave frequencies (currently, the device shows no response at frequencies below 0.60 Hz). At lower frequencies the period of motion increases and this allows more time for the flaps to operate. Finally, the performance evaluations discussed in Chapter 4 were done in monochromatic wave trains. The prototype should also be studied in ocean specific broadband spectra.

5.3 Closing Remarks

We believe that with this research work we have introduced a novel idea in the field of ocean wave energy converters. On one hand, this field has been an established one for some time. On the other, it is still relatively young in terms of working prototypes. We hope that our contribution helps advance the art and science of ocean wave energy converters and brings them closer to being grid-connected sources of clean, renewable energy.

As with most novel ideas that have to be physically demonstrated, it is a challenge to create a perfectly working example in the beginning. In our case, it took three different attempts to construct a prototype that functioned in a satisfactory manner. However, we believe that with the results presented in this dissertation a suitable amount of groundwork has been laid to further develop the concept of mass modulation in ocean wave energy converters.

References

[1] 2007 Survey of Energy Resources. URL http://www.worldenergy.org. World Energy Council

[2] Badour, E.: Energy from waves and tidal currents towards 20yy? (2004). URL http://www.nrc-cnrc.gc.ca/eng/ibp/iot.html. Institute for Ocean Technology, National Research Council

[3] Billah, K.: On the definition of parametric excitation for vibration problems. Journal of Sound and Vibration **270**(1-2), 450–454 (2004). URL http://dx.doi.org/10.1016/S0022-460X(03)00408-5

[4] Butikov, E.I.: Parametric excitation of a linear oscillator. European Journal of Physics **25**(4), 535–554 (2004). URL http://dx.doi.org/10.1088/0143-0807/25/4/009

[5] Butikov, E.I.: Parametric resonance in a linear oscillator at square-wave modulation. European Journal of Physics **26**(1), 157–174 (2005). URL http://dx.doi.org/10.1088/0143-0807/26/1/016

[6] Clément, A., McCullen, P., Falcão, A., Fiorentino, A., Gardner, F., Hammarlund, K., Lemonis, G., Lewis, T., Nielsen, K., Petroncini, S., et al.: Wave energy in Europe: current status and perspectives. Renewable and Sustainable Energy Reviews **6**(5), 405–431 (2002)

[7] De Backer, G., Vantorre, M., Banasiak, R., De Rouck, J., Beels, C., Verhaeghe, H.: Performance of a point absorber heaving with respect to a floating platform. 7th European Wave and Tidal Energy Conference. Porto (2007)

[8] Di Bernardo, M.: Piecewise-Smooth Dynamical Systems: Theory and Applications. Springer Verlag (2008)

[9] Di Bernardo, M., Budd, C., Champneys, A., Kowalczyk, P., Nordmark, A., Tost, G., Piiroinen, P.: Bifurcations in nonsmooth dynamical systems. SIAM Review **50**, 629 (2008). URL http://dx.doi.org/10.1137/050625060

[10] Evans, D.V.: A theory for wave-power absorption by oscillating bodies. J. Fluid Mech. **77**(1), 1–25 (1976). URL http://dx.doi.org/10.1017/S0022112076001109

[11] Flieller, D., Riedinger, P., Louis, J.: Computation and stability of limit cycles in hybrid systems. Nonlinear Analysis **64**(2), 352–367 (2006). URL http://dx.doi.org/10.1016/j.na.2005.06.054

[12] Gonçalves, J.M.: Regions of stability for limit cycle oscillations in piecewise linear systems. IEEE Transactions on Automatic Control **50**(11), 1877–1882 (2005). URL http://dx.doi.org/10.1109/TAC.2005.858674

[13] Hiskens, I.: Stability of hybrid system limit cycles: Application to the compass gait biped robot. In: Decision and Control, 2001. Proceedings of the 40th IEEE Conference on, vol. 1, pp. 774–779. IEEE (2002). URL http://dx.doi.org/10.1109/.2001.980200

[14] Hiskens, I., Reddy, P.: Switching-induced stable limit cycles. Nonlinear Dynamics **50**(3), 575–585 (2007). URL http://dx.doi.org/10.1007/s11071-006-9175-0

[15] Johansson, M.: Piecewise Linear Control Systems. Ph.D. thesis, Lund Institute of Technology (1999)

[16] Leishman, J., Scobie, G.: The development of wave power: a techno-economic study. National Engineering Laboratory, Economic Assessment Unit (1980)

[17] Liberzon, D.: Switching in Systems and Control. Systems & Control: Foundations & Applications. Birkhäuser, Boston, MA (2003)

[18] Liberzon, D., Morse, S.A.: Basic problems in stability and design of switched systems. IEEE Control Systems Magazine **19**, 59–70 (1999)

[19] Mei, C.C.: Power extraction from water waves. J. Ship Research **20**(2), 63–66 (1976)

[20] Olvera, A., Prado, E., Czitrom, S.: Parametric resonance in an oscillating water column. Journal of Engineering Mathematics **57**(1), 1–21 (2007). URL http://dx.doi.org/10.1007/s10665-006-9048-z

[21] Orazov, B., O'Reilly, O.M., Savaş, Ö.: On the dynamics of a novel ocean wave energy converter. Journal of Sound and Vibration **329**(24), 5058–5069 (2010). URL http://dx.doi.org/10.1016/j.jsv.2010.07.007

[22] Orazov, B., O'Reilly, O.M., Zhou, X.: On forced oscillations of a simple model for a novel wave energy converter: Non-resonant instability, limit cycles, and bounded oscillations. Nonlinear Dynamics pp. 1–12 (2011). URL http://dx.doi.org/10.1007/s11071-011-0058-7. Accepted for publication

[23] Rhoads, J.F., Miller, J.N., Shaw, S.W., Feeny, B.F.: Mechanical domain parametric amplification. Journal of Vibration and Acoustics **130**(6), 061,006–1–061,006–7 (2008). URL http://dx.doi.org/10.1115/1.2980382

[24] Rubensson, M., Lennartson, B.: Global convergence analysis for piecewise linear systems applied to limit cycles in a DC/AC converter. pp. 1272–1277. Anchorage, Alaska, May 8–10, 2002 (2002). URL http://dx.doi.org/10.1109/ACC.2002.1023195

[25] Rubensson, M., Lennartson, B.: Stability of limit cycles in hybrid systems using discrete-time Lyapunov techniques. In: Decision and Control, 2000. Proceedings of the 39th IEEE Conference on, vol. 2, pp. 1397–1402. IEEE (2002). URL http://dx.doi.org/10.1109/CDC.2000.912053

[26] Rugar, D., Grütter, P.: Mechanical parametric amplification and thermomechanical noise squeezing. Physical Review Letters **67**(6), 699–702 (1991). URL http://dx.doi.org/10.1103/PhysRevLett.67.699

[27] Salter, S.H.: Wave power. Nature **249**, 720–724 (1974). URL http://dx.doi.org/10.1038/249720a0

[28] Spain, R.: A possible Roman tide mill. Kent Archaeological Society, paper **5** (2002). URL http://www.kentarchaeology.ac/authors/005.pdf

[29] Stephen, N.G.: On energy harvesting from ambient vibration. Journal of Sound and Vibration **293**(1–2), 409–425 (2006). URL http://dx.doi.org/10.1016/j.jsv.2005.10.003

[30] Watt, D., Cartmell, M.P.: Externally loaded parametric oscillator. Journal of Sound and Vibration **170**(3), 339–364 (1994). URL http://dx.doi.org/1006/jsvi.1994.1067

[31] Whitham, G.: Linear and nonlinear waves, vol. 226. Wiley New York (1974)